



Temperature profiles combined from lidar and airglow measurements

Thomas Trickl¹, Hannes Vogelmann¹, Michael Bittner^{2,5}, Gerald Nedoluha³, Carsten Schmidt², Wolfgang Steinbrecht⁴ and Sabine Wüst²

¹Karlsruher Institut für Technologie, Institut für Meteorologie und Klimaforschung (IMK-IFU), Kreuzeckbahnstr. 19, 82467 Garmisch-Partenkirchen, Germany

²Deutsches Zentrum für Luft und Raumfahrt (DLR), Deutsches Fernerkundungsdatenzentrum (DFD), 82234 Oberpfaffenhofen, Germany

³Naval Research Laboratory, 4555 Overlook Avenue, SW, Washington, D.C. 20375, U.S.A.

⁴Deutscher Wetterdienst, Meteorologisches Observatorium Hohenpeißenberg, Albin-Schwaiger-Weg 10, 82383 Hohenpeißenberg, Germany

⁵Universität Augsburg, Institut für Physik, 86159 Augsburg, Germany

Correspondence to: Dr. Thomas Trickl, thomas@trickl.de, Thomas-Knorr-Str. 47, D-82467 Garmisch-Partenkirchen, Germany; tel. +49-8821-50283; Dr. Hannes Vogelmann, hannes.vogelmann@kit.edu, Karlsruher Institut für Technologie, IMK-IFU, Kreuzeckbahnstr. 19, D-82467 Garmisch-Partenkirchen, Germany; tel.: +49-8821-258

Abstract. In this study we examine the performance of the 354.8-nm Rayleigh temperature channel of the Raman lidar at the Schneefernerhaus high-altitude research station (UFS) in the Bavarian Alps (at 2675 m a.s.l.). The temperature reference value of the retrieval is adjusted to match the temperature determined from the OH* airglow around 86 km by the GRIPS instruments at UFS. In this way the quality of the 1-h measurements of the lidar is improved above 70 km. Comparisons were made between the UFS lidar, the MLS (Microwave Limb Sounder) satellite-borne instrument and the 354.8-nm temperature channel of Hohenpeißenberg (MOHp) differential-absorption ozone lidar. Between 35 km and 70 km we see a positive offset of the UFS temperatures with respect to the MLS values of up to about 9 K. This behaviour just slightly exceeds the expectations from earlier work. Despite a horizontal distance of just 40 km between UFS and MOHp acceptable agreement below 70 km was found in several cases. However, in general, the MOHp temperatures were slightly lower than those above UFS. We discuss potential technical issues and suggest solutions for upgrading the UFS lidar system. A significant enhancement of the laser repetition rate is recommended.

Key words: Temperature, stratosphere, mesopause, lidar, MLS, OH, airglow

1. Introduction

Accurate temperature measurements at short time intervals up to the mesosphere are an important contribution to climate research and for a better understanding of the atmospheric energy balance, in particular with respect to gravity waves. This can yield information for improving atmospheric and climate models that usually only consider the comparatively small-scale gravity waves in the form of parameterizations (e.g. Kim et al., 2003; Medvedev et al., 2019). These are simplified mathematical formulations of the wave effects, as exact calculations are hardly possible for resource reasons.

In the lower atmosphere the vertical distribution of the temperature is mostly obtained from the routine radiosonde ascents that are typically carried out up to roughly 30 km twice per day. Routine measurements up to higher altitudes are to a major extent provided by satellite-based sensors yielding temperature profiles up to more



than 90 km (e.g., Curtis et al., 1974; Russell et al., 1999; Waters et al., 2006;). These measurements are carried out with a rather dense global coverage.

These observations are complemented by ground-based lidar measurements. Leblanc et al. (1998) stated that lidar measurements provide the best vertical resolution and accuracy for middle-atmosphere temperature studies. The most commonly applied lidar method is based on Rayleigh scattering (e.g., Hauchecorne and Chanin, 1980; Hauchecorne et al., 1991; Fishbein et al., 1996; von Zahn et al., 2000; Keckhut, 2004) and yields temperatures typically in the mostly aerosol-free range between 30 and 85 to 95 km. The temperature inversion from Rayleigh backscatter profiles is the key approach within the global Network for the Detection of Atmospheric Composition Change (NDACC, <https://ndacc.larc.nasa.gov>). Also, daytime measurements, based on extremely narrowband spectral filtering and a very small field of view, have been demonstrated (e.g., Gille et al., 1991; von Zahn et al., 2000).

The measurements times can be excessive and must be reduced to capture the short-term temperature variability. This is achieved by the use of a powerful laser and a large receiver. Sica et al. (1995) have used a 2.65-m-diameter spinning liquid-mercury mirror in order to collect a maximum of 532-nm light backscattered from 12 W from a frequency-doubled Nd:YAG laser and, in this way, have achieved temperature measurements up to more than 100 km within 6 h of lidar operation and with vertical bin sizes of 48 m. At lower altitudes, shorter measurement times are possible. The propagation of tidal and gravity waves was visualized in the altitude range between 33 and 50 km (Sica, 1999).

Traditionally, backward retrievals starting at the highest useful altitude are applied (Hauchecorne and Chanin, 1980). This approach converges to the correct solution within roughly 15 km. In order to obtain more quantitative data also in the uppermost range forward retrievals based on optimum-estimation methods have been successfully applied (Khanna et al., 2012).

Above 80 km fluorescence lidar methods are used both for density and temperature measurements, up to 110 km. The sensitivity of laser-induced fluorescence methods is very high and has made possible single-atom detection in the laboratory (e.g., Ott, 2016). In the atmosphere its application is limited to low-density conditions where fluorescence quenching is avoided. Metallic species, in particular sodium, potassium and iron atoms, have been successfully detected and used for temperature retrievals (e.g., Bowman et al., 1969; Blamont et al., 1972; Mégie et al., 1978; Fricke and von Zahn, 1985; Granier et al., 1989; She et al., 1990; Papen et al., 1995; Arnold and She, 2003; Xu et al., 2006). This method has allowed for daytime operation (e.g., Chen et al., 1996; Chu et al., 2001; Höffner and Lautenbach, 2009).

A combination of all the three lidar methods (rotational Raman scattering (e.g., Arshinov et al., 1983; Behrendt, 2005; Serikov and Bobrinikov, 2009), fluorescence, and Rayleigh scattering) has been applied to generate a composite temperature profile from 1 km to 105 km (Alpers et al., 2004). This approach has been extended to daytime operation by narrowband spectral filtering (Gerding et al., 2010; Kopp et al., 2015; see also von Zahn et al., 2000). The propagation of waves could be studied in an enormous range between 35 km and 104 km.

Alternatively, temperature information has been obtained from ground-based measurements of the OH* airglow (e.g., Sivjee, 1992; Scheer et al., 1994; Bittner et al., 2000; 2002; Beig et al., 2003; Reisin et al., 2014; Wüst et al., 2023). This method is not height resolved, but benefits from the rather confined range of the OH* airglow with its peak emission height between 85 and 87 km and a full width at half maximum (FWHM) between 6 and 9 km on average for the Alpine region (Wüst et al., 2017). Peak emission height and FWHM show an annual and a semi-annual variation due to vertical transport processes at this height. Latitudinal and longitudinal variations exist to a small extent (Wüst et al., 2020). Those values are retrieved from multi-year satellite data. From



83 ground-based OH* airglow measurements some height information can be deduced based on the altitude-
84 dependence of the vibrational population (e.g., Lopez-Moreno et al., 1987; von Savigny et al., 2012; Schmidt et
85 al., 2018, Noll et al., 2023)) or from the relation between the column-integrated volume emission rate and peak
86 emission height (e.g., Liu and Shepherd, 2006; Mulligan et al., 1995). The second method is based on the
87 functional relationship between both parameters; this must first be determined, e.g., by adding height-resolved
88 satellite measurements. In addition, the OH* layer has frequently been observed in limb geometry by rocket- and
89 satellite-borne spectrometers or radiometers (e.g., Baker and Stair, 1988; Takahashi et al., 1996; Englert et al.,
90 2010; von Savigny et al., 2013; Noll et al., 2017; Wüst et al., 2017; Li et al., 2021). Von Zahn et al. (1987), She
91 and Lowe (1998) and Schmidt et al. (2018) compared temperature measurements of sodium lidar systems with
92 results from OH* spectrometers. It should be noted that ground-state ($v'' = 0$) OH molecules have been observed
93 by laser-induced ultraviolet fluorescence, i.e. in the $A^2E^+ - X^2II(0, 0)$ band at heights between 75-85 km
94 (Brinksma et al., 1998). The chemiluminescent OH*-layer addressed by passive remote sensing instruments
95 consists of pure rotational-vibrational transitions ($v'' \leq 9$) within the X^2II electronic state and, originating from a
96 different chemical reservoir, and peaks at higher altitudes (see Baker and Stair, 1988; Wüst et al., 2017).

97 In 2018 measurements of the atmospheric temperature in the stratosphere and the mesosphere were started with
98 the 355-nm channel of the big Raman-Rayleigh lidar system at the Schneefernerhaus Alpine high-altitude station
99 (UFS, 2675 m a.s.l.) in the Bavarian Alps (Klanner et al., 2021). These activities extend the water-vapour
100 (Vogelmann and Trickl, 2008) and aerosol (Trickl et al., 2024) sounding at this site. The backscatter profiles,
101 acquired within one hour, currently cover a range up to roughly 90 km. The inversion of these profiles yields
102 temperature data up to more than 80 km if a reliable upper-end temperature reference is available. At UFS we
103 benefit from using the temperature data from the OH* measurements at the station as a reference. This is a clear
104 advantage with respect to comparisons with satellite data, obtained on somewhat remote orbits, or with models
105 of unknown reliability (see Klanner et al., 2021).

106 In this paper, we aim at validating this new instrument, a task mandatory because of the features of the large
107 detection system and in view of the planned archiving in the data base of the Network for the Detection of
108 Atmospheric Composition Change (NDACC, <https://www.ndacc.org>). We look for the principal performance
109 and, thus, just give comparisons with a limited number of instruments carefully characterized elsewhere (for
110 references see below). In particular, we judge the performance by nearby lidar measurements and derive
111 recommendations for improvements and further tests.

112 2. Data sources

113 2.1 Rayleigh backscatter measurements at 354.8 nm with a large lidar system at the Schneefernerhaus 114 high-altitude station (Zugspitze, Germany)

115 Since 2009 a high-power Raman lidar system has been developed by a team from the Institute for Atmospheric
116 Environmental Research (Garmisch-Partenkirchen, Germany; since 2009 Karlsruher Institute of Technology,
117 IMK-IFU) that yields profiles of the water-vapour mixing ratio up to more than 20 km within one hour (Klanner
118 et al., 2021). This lidar is located at the high-altitude station Schneefernerhaus (Umweltforschungsstation
119 Schneefernerhaus, UFS, 47° 25' 00" N, 10° 58' 46" E, 2675 m a.s.l.) on the south side of Mt. Zugspitze (2962 m
120 a.s.l.), about 9 km to the south-west of IMK-IFU. Because of its elevation UFS provides mostly free-
121 tropospheric conditions (Carnuth et al., 2002). As pointed out by Trickl et al. (2024) the high base elevation
122 yields a significant gain in backscatter signal even in the stratosphere. The system is operated side by side with a
123 differential-absorption water-vapour lidar (DIAL; Vogelmann and Trickl, 2008; Trickl et al., 2014; 2015; 2016)



124 which allows for optimum calibration, also considering an absence of a significant bias, at least within the first
125 kilometres (Vogelmann et al., 2011; Trickl et al., 2016).

126 The Raman lidar system benefits from a large Newtonian receiver with 1.5 m diameter and a XeCl laser with up
127 to 180 W emission in single-line operation at a repetition rate of 350 Hz (Coherent, Lambda SX, with an
128 extended cavity containing an intracavity etalon and a polarizer).

129 This system can additionally yield temperature measurements by two methods. Up to the lower stratosphere the
130 temperature may be retrieved from two rotational Raman channels. This approach has been successfully tested
131 (Höveler, 2015), but has not yet entered routine operation because the focus has so far been on optimizing the
132 performance of the H₂O channel.

133 The second approach is inverting one of the two Rayleigh backscatter profiles of the lidar at 307.96 nm and
134 353.14 nm. The emission for the preferred second channel was first generated by stimulated Raman shifting the
135 output of the XeCl laser in hydrogen (Klanner, 2022). However, the performance at 353.14 nm was not reliable
136 at the high repetition rate of 300 Hz. As a consequence we added a frequency-tripled injection-seeded Nd:YAG
137 laser (Continuum, Powerlite Precision 8020) previously used in our water-vapour DIAL. This laser emits at the
138 wavelength of 354.81233 nm and yields pulse energies of 170 mJ, substantially more than the emission planned
139 from the Raman-shifted excimer laser. However, the repetition rate is limited to 20 Hz. The choice of the
140 ultraviolet wavelength provides the advantages of a larger backscatter signal than for 532.2 nm. Most
141 importantly, the light-absorption by ozone at 532.2 nm is avoided (Trickl et al., 2024).

142 A general design feature in our lidar systems is the absence of optical fibres. In this way, coupling losses, near-
143 field issues and fluorescence effects are avoided. In addition, the polarization of the transmitted radiation is
144 conserved which is essential for the chosen optical configuration of the detection polychromator (Fig. 8 of
145 Klanner et al., 2021). The 354.8-nm channel is spectrally filtered by a combination of a filter (Semrock),
146 transmitting 85 % – 90 % of the radiation between 330 and 355 nm and blocking spectral contributions outside
147 this range by at least 10⁵, and a narrowband filter with a width of less than 1.2 nm (Alluxa).

148 A key issue for temperature measurements is a high quality of the detection electronics: An uncertainty of (e.g.)
149 the order of 1 K means a relative uncertainty of the measurements of less than 0.5 %. Here, we benefit from the
150 experience gained from our older systems (e.g., Trickl et al., 2020; 2023; 2024). The backscattered radiation is
151 detected with Hamamatsu R7400U-03 photomultiplier tubes (PMTs) with actively stabilized sockets from
152 Romanski sensors (RSV). In the following we describe, for simplicity, the signal voltages as positive values
153 instead of the negative ones emerging from the detectors. The performance of these detectors is highly linear for
154 peak analogue signals cautiously set to 70 mV and less (Trickl et al., 2020; 2024). Here, this is achieved by
155 adjusting the laser pointing in order to maintain the maximum far-field signal level. However, the analogue
156 output is ten times more sensitive to the background signal than the PMTs from the older 5400 series (Trickl et
157 al., 2020). Undershooting occurs at analogue background levels exceeding 1 mV (for 50 Ω termination), which
158 does not matter during night-time. However, also excessive lidar backscatter could, in principle, lead to some
159 undershooting and we have, therefore, limited the peak analogue signal even to less than the 70 mV (into 50 Ω)
160 successfully applied by Trickl et al. (2020).

161 The output is registered in 12-bit transient digitizers at a range-bin size of 7.5 m (Licel). This model was
162 modified in 2010 for our ozone DIAL with a ground-free input, which was also implemented in all systems
163 digitizer systems purchased in the following. The Licel transient digitizer is optimized for very low noise (less
164 than ±10⁻⁵ of the measurement range for 4096 laser shots), but, in contrast to the previously used system from
165 DSP Technology (model DSP 2020; Trickl et al., 2020), features a slight exponential wing that grows with the



166 area of the lidar backscatter signal. This wing could be easily corrected in the case of the ozone DIAL because of
167 the short decay time of the signal (Trickl et al., 2020), but is difficult to quantify for the long signal at longer
168 wavelengths. An exponential curve is subtracted, derived from a comparison with the photon-counting results at
169 high altitudes. The decay constant is the same for all retrievals.
170 Parallel to this detection channel for the analogue signal we count the individual photons in a MCS6a
171 multichannel scaler (FAST ComTec) with a pulse-pair resolution of 0.2 ns, more than sufficient for the 1.5-ns-
172 wide pulses from the detector. Because of the near-field overload of the sequential data transfer to the computer
173 we delay the start of the counting system by 10 μ s. The perfect linearity of the photon-counting channels has
174 been verified by the validation of our water-vapour measurements (Klanner et al., 2021) and the performance of
175 our stratospheric aerosol measurements (Trickl et al., 2024), at least to up to 45 km. We have been optimistic
176 that the perfect linearity extends to much higher altitudes since the settling time of artefacts for this type of PMT
177 seems to be rather short. For the threshold voltage of -4 mV set at the fast discriminator (RSV) testing with
178 closed detector entrance revealed that the detection is free of “dark counts”. For the temperature measurements,
179 the night-time background count rate is of the order of 0.2 counts per 7.5-ns bin and hour at the maximum
180 distance of 120 km, which allows for keeping the far-field signal-to-noise ratio as high as possible.

181 **2.2 Microwave Limb Sounder on board the Aura satellite**

182 The Microwave Limb Sounder (MLS; Waters et al., 2006) on board the Aura satellite (Schoeberl et al., 2006)
183 was launched to space in 2003. The instrument not only detects thermal emission from various molecules (most
184 recently, e.g., Nedoluha et al., 2024; 2025), but also yields vertical profiles of the atmospheric temperature up to
185 almost 100 km. 3500 vertical profiles are produced per day. The temperature retrieval is based on limb radiances
186 near the oxygen spectral lines at 118 GHz and 234 GHz. The limb-tangent pressure is derived from the shape of
187 the broadened O₂ lines.
188 Schwartz et al. (2008) analysed the quality of the temperature and geopotential height determined from the
189 measurements. Comparisons with other satellite-borne instruments indicate a negative temperature bias for
190 altitudes corresponding to pressures of 1 mbar and less. Mevedewa et al. (2014) report a negative bias of about
191 -10 K of the MLS temperature with respect to that obtained from OH measurements above 80 km.
192 For the examples shown in this paper there are just two of the 14 cases with a passage almost perfectly above
193 Garmisch-Partenkirchen during the night-time lidar observations. Given the enhanced wave activity that can be
194 expected above the Alps (e.g., Hannawald et al., 2019) this limits the quality of comparisons.
195 The geopotential height is converted to absolute height for the comparisons.

196 **2.3 GRIPS OH* chemiluminescence**

197 A closer spatial agreement with the UFS lidar is achieved with the routine OH* airglow measurements at UFS in
198 the mesopause region. The OH spectra are registered with the Ground-based Infrared P-branch Spectrometer
199 (GRIPS) instrument (Schmidt et al., 2013), integrated in the global Network for the Detection of Mesosphere
200 Change (NDMC; <https://ndmc.dlr.de>; e.g., Reisin et al., 2014). The centroid altitude of the airglow is 86 ± 2 km
201 and slightly varies with the season (von Zahn et al., 1987; Baker and Stair, 1988; She and Lowe, 1998; Wüst et
202 al., 2017, 2020). The aims of the research are an identification and quantification of the influence of climate
203 change, the detection of solar activity effects, the influence of atmospheric dynamics (wave activity) and the
204 validation of satellite instruments.



205 A survey on the relevant spectroscopic data and literature is given, e.g., by Noll et al. (2020) and Wüst et al.
206 (2023). Wüst et al. (2023) provide a review on the recent achievements of OH* measurements. Only transitions
207 emerging from low-lying vibrational levels appear to be suitable for sufficiently quantitative temperature
208 derivations and we, therefore, use the low-lying (3,1) OH* transitions (Bittner et al., 2002; Noll et al., 2017). The
209 lack of vertical resolution and the relatively large thickness of the OH* layer yields temperatures that are
210 weighted means over a layer of the atmosphere extending over roughly 8 km.

211 The GRIPS instrument at UFS is oriented for slant-path detection which means that the OH* layer is reached
212 approximately above Bozen (46.6° N, 11.0° E, Italy) south of the Central Alps, at a horizontal distance of
213 roughly 90 km. The night-time temperature time series exhibit variations such as can be seen in the three
214 examples shown in Fig. 1. The amplitudes of the T variations can be as high as 10 K, rarely more. In order to
215 gain insight into the horizontal extent of these structures we, therefore, compared the GRIPS measurements with
216 those at Oberpfaffenhofen (OPN, 48.1°N, 11.3°E, about 77 km to the north) during the same nights. The full-
217 night average temperatures at both sites mostly agree within 1 to 3 K. The structures measured from the OPN
218 station are not identical, but at least similar (see right panels in Fig. 1). The cases with pronounced differences
219 demonstrate that temperature changes can occur on a confined spatial scale. This leads to uncertainties for the
220 comparisons in Sect. 3.

221 The temperature exhibits a pronounced seasonal dependence varying between about 170 K in summer and 220 K
222 in winter, with average amplitudes of 17.5 K and 3.0 K of the annual and semi-annual component (see Schmidt
223 et al., 2023). There is no consistent trend in the night-time series used this study, but a general tendency for a
224 slight rise. Systematic temperature changes throughout the night caused by the semidiurnal migrating (12 h) tide,
225 maximising in winter can be expected. On average this can lead to a 4-5 K temperature increase from 21 CET to
226 3 CET at UFS in January (compare Fig. 7 in Schmidt et al (2023)). As far as the nights used in this study show
227 variability at all, it appears to be dominated by shorter period structures, which in some cases exhibit substantial
228 amplitudes (compare Figure 2).

229 **2.4 Temperature measurements with the Hohenpeißenberg ozone DIAL**

230 A considerable chance for the validation of the UFS lidar is given by the routine night-time temperature
231 measurements with the ozone differential-absorption lidar (DIAL) at the Meteorological Observatory Hohen-
232 peißenberg (MOHp) of the German Weather Service. This station is located just 42 km to the north of UFS.

233 The MOHp DIAL is technically similar to the UFS lidar (Wing et al., 2021) which is an excellent basis for
234 comparisons. For the T measurements it is also operated at 354.8 nm using a frequency-tripled Nd:YAG system
235 (Innolas, model SpitLight 600, 120 mJ per pulse, 20 Hz repetition rate). The PMT type is similar (Hamamatsu,
236 R9880U-110, with home-made socket) and was compared with the PMT type used at UFS without showing a
237 difference in lidar backscatter profile. The diameter of the principal mirror of the Newtonian telescope is smaller
238 (1.0 m), but the data acquisition is extended to full nights, which results in a high signal-to noise ratio.
239 Exclusively photon counting is applied (FAST, P7882-2, maximum count rate 200 MHz).

240 The data are averaged over 150 m and, after the evaluation, smoothed to 450 m. The temperatures are routinely
241 stored in the NDACC data base (<https://ww-air.larc.nasa.gov/missions/ndacc/data.html#>) from 27 km to roughly
242 95 km.

243 **3. Inversion of the UFS lidar data**



244 3.1 Temperature retrieval

245 The temperature profiles are retrieved from the 354.8-nm backscatter profiles as described by Klanner et al.
246 (2021). Here, we give a few more details than in the preceding publication, based on the experience gained from
247 the more recent measurements.

248 The algorithm is a modified version of the downward inversion method introduced by Hauchecorne and Chanin
249 (1980; see also Shibata et al., 1986). This method has the advantage of self-correction within roughly 15 km
250 from the top (reference) altitude and is less complicated than the forward inversion proposed by Khanna et al.
251 (2012) which might be implemented at a later stage. However, we benefit from the OH* airglow measurements
252 at UFS that allow us to shift the reference temperature to a value that yields a good match of the T profile with
253 the OH temperature at 86 km, the average altitude of the OH* layer (Wüst et al., 2017). In cases in which the
254 reference altitude has to be chosen below 86 km an extrapolation is estimated. In cases in which the reference
255 altitude is above 86 km we used the temperature from the U.S. Standard Atmosphere (1976) in a first step and
256 apply a correction in a following retrieval that shifts the temperature at 86 km to a value within the uncertainty
257 range of the GRIPS temperature.

258 The main source of data is the photon-counting signal. We select a bin size of 51.2 ns, which represents a length
259 of 7.6747 m. The PMTs were tested without input radiation and turned out to be free of background counts for 1
260 h of data accumulation in a single bin. Thus, no cooling of the detector is required. As mentioned, in night-time
261 atmospheric measurements the average background count rate has been as low as roughly 0.2 counts bin⁻¹ h⁻¹
262 (Fig. 1). This is the result of careful spatial filtering and the narrow spectral filtering. This performance to a
263 major extent excludes artefacts such as those described by Wing et al. (2018a). The backscatter profiles from the
264 counting system are interpolated to match the 7.4948 m bin size and the vertical grid of the transient digitizer.

265 We start the data evaluation with visualizing the raw data and their conversion. In Fig. 1 we show an example of
266 backscatter profiles from 9 October 2021. After determining the zero point of the distance scale we average the
267 content of two neighbouring bins and double the size of a single data bin to 14.9896 m, which reduces the
268 number of bins to 8000 (119.917 km). The analogue data are substantially noisier than the photon-counting data
269 and exhibit a background drift tentatively ascribed to the performance of the transient digitizer. The 355-nm
270 analogue profile was corrected by subtracting $3.22 \times 10^{-4} \exp(-8.0 \times 10^{-6} \times r)$, with r being the distance above the
271 lidar in metres. The constant of the exponential decay was used in all measurements evaluated since April 2021.
272 This decay is 7 times slower in comparison with that in our ozone DIAL (Trickl et al., 2020) and is observable
273 just because of the excessive operating range and the longer averaging. The fast decay component of the DIAL
274 (277 to 313 nm) cannot be resolved because of the slower decay of the 355-nm signal, also implying the absence
275 of absorption in ozone.

276 The analogue data are used from about 10 km to 30 km. As can be seen in Fig. 1 the correction is crucial for
277 obtaining optimum temperature profiles from the analogue data for distances r up to 30 km. The data correction
278 must be made with care because of the enormous requirements for the temperature measurements. Below 10 km
279 the signal is partially cut off by one side (blade) of the entrance aperture, the laser beam being adjusted to limit
280 the near-field peak signal. Above 30 km the photon-counting signal is taken where it is fully linear. No dead-
281 time correction has been implemented in this channel as frequently done in lidar systems based on counting
282 alone. All backscatter signals are carefully compared with simulations from meteorological data (see also
283 below).

284 The analogue measurement in Fig. 1 is the best in comparison with those in the other measurements obtained
285 since spring 2021. In other cases, slight deviations from the clean exponential behaviour were observed that we



286 tend to ascribe to interference of the magnetic field of the laser flashlamps as found in earlier work (e.g., Trickl ,
287 2010). The use of a diode-laser-pumped laser system is planned (see Sect. 4). For such a laser system we have
288 not found any similar interference (Trickl et al., 2024).
289 For reducing the data noise we apply altitude-depended smoothing with a numerical filter as described by Trickl
290 et al. (2020). The bin interval of the Blackman-type filter is nonlinearly enhanced using the formula
291 $a + i^2 \times b$
292 at bin i (size 14.9896 m), with normally $a = 20$ and $b = 4 \times 10^{-5}$. This results in a variation of the VDI (1999)
293 vertical resolution from 58 m at the ground to 1216 m at 50 km and a maximum of 2908 m at and above 76.7 km
294 a.s.l. (Trickl et al., 2020; VDI, 1999; see (Iarlori et al., 2015; Leblanc et al., 2016) for other definitions). The
295 VDI resolution is defined as the range difference between 25 % and 75 % of the response to a Heaviside step.
296 Above this, the vertical resolution stays constant to limit the computation requirement.
297 As described by Klanner et al. (2021) we first calculate the atmospheric density in a fully quantitative Klett-type
298 approach with downward integration from the far end (Klett, 1981; 1985):

$$299 \quad n(r) = \frac{n(r_{ref}) r_{ref}^2 S(r_{ref})}{r^2 S(r) + 2n(r_{ref}) \sigma_R \left[\int_r^{r_{ref}} r'^2 S(r') dr' \right]}, \quad (1)$$

300 $S(r)$ being the backscatter signal, r_{ref} the reference distance and σ_R the Rayleigh extinction coefficient. Here, the
301 misprint in Eq. 1 of Klanner et al. (2021) is corrected that has not been part of the computer program. The far-
302 end reference density $n(r_{ref})$ is varied for matching the density derived from the Munich radiosonde (launched at
303 Oberschleißheim, station 10868, about 100 km roughly to the north), also making comparisons with the densities
304 from NCEP (National Centers for Environment Prediction) at higher altitudes. We download the sonde data from
305 <https://weather.uwyo.edu/upperair/sounding.html>. The NCEP altitudes, pressures and temperatures are taken
306 from the web site of the Network for the Detection of Atmospheric Composition change as calculated for
307 Garmisch-Partenkirchen (<https://www-air.larc.nasa.gov/missions/ndacc/data.html?NCEP=ncep-list>). The NCEP
308 listings are available up to roughly 55 km.

309 From the density n we obtain the temperature profile by applying

$$310 \quad T(z) = T(z_0) \frac{n(z_0)}{n(z)} + \frac{m_{air}}{k n(z)} \int_z^{z_0} n(z') g(z') dz', \quad (2)$$

311 with z being the altitude above sea level, z_0 the far-end reference altitude, $m_{air} = 28.9644$ u (U.S. Standard
312 Atmosphere, 1976; $1 \text{ u} = 1.66053904 \times 10^{-27}$ kg (Mohr et al., 2016)) the mass of an “average air molecule”, and g
313 the gravitational acceleration,

$$314 \quad g(z) = g_0 \left(\frac{r_E}{r_E + z} \right)^2,$$

315 with $g_0 = 9.80665 \text{ m s}^{-1}$ and the earth radius $r_E = 6356766 \text{ m}$ (U.S. Standard Atmosphere, 1976). In the U.S.
316 Standard Atmosphere the atmosphere is regarded as well mixed up to 86 km, which suggests to be cautious at
317 the highest altitudes accessible.

318 The inversion starts at the highest reasonable altitude, mostly below the upper end of the density profile.
319 Normally, we take the temperature for the start altitude from the U.S. Standard Atmosphere (1976) as the
320 reference. The algorithm in Eq. 2 is self-correcting: Within 15 km of downward integration the temperature is



321 does no longer vary as a function of the reference value by more than ± 2 K (Klanner et al., 2021), as a
322 consequence of the density dependence of the first term of Eq. 2. It turned out that the influence of the reference
323 density (Eq. 1) is very low and can be neglected for the careful adjustment made (see above).
324 In eight of the fourteen cases examined we had to make adjustments of the reference temperatures to match the
325 temperature of the GRIPS instrument at 86 km, or, in one case without GRIPS measurements, the range of MLS
326 values. For a perfect comparison of lidar and GRIPS an extension of the operating range of the lidar to more than
327 100 km is desirable. Wing et al. (2018a) recommended to use the MSIS model output as a reference. The result
328 was not satisfactory at all (Klanner et al., 2021) and we decided to use the GRIPS temperatures.
329 The retrieval of temperature from lidar data is a highly demanding task. For instance, an uncertainty of 1 K
330 means a relative uncertainty of 0.33 % at a temperature of 300 K. Thus, a very high quality of the backscatter
331 signals is a prerequisite for reasonable results.
332 Aerosol corrections have been tested and lift the temperature in a range around 22 km, typically by 2 to 4 K
333 under the conditions of the cases chosen. The aerosol backscatter coefficients are taken from the stratospheric
334 aerosol measurements (Trickl et al., 2024) from adjacent days and converted from 532.24 nm to 354.8 nm by
335 multiplication with 1.992 (Jäger and Deshler, 2002; 2003). However, such an effort makes sense just if the
336 quality of the exponentially corrected analogue signal matches that in Fig. 1 which was the case just for two
337 measurements (16 November 2018 and 9 October 2021). In the other cases, the analogue signal background
338 exhibited slight modulations perhaps caused by the magnetic field of the flashlamp-pumped laser. Here, the
339 exponential correction is adjusted to generate temperature values matching those from the midnight Munich
340 radiosonde (station 10868).

341 3.2 Uncertainties

342 As pointed out in the U.S. Standard Atmosphere (1976) the atmospheric composition is homogeneous mixed up
343 to 86 km. Local short-term perturbations are averaged away by the long signal acquisition time of 1 h.
344 The uncertainty from shot noise, as derived from the smoothed signal, is of the order of 10 K at 70 km. We use a
345 scaling law

$$346 \quad u = \sqrt{u_0^2 + \left(u_1 \frac{r^2}{r_{\text{ref}}^2}\right)^2 + (u_2 S(r))^2}, \quad (3)$$

347 for the uncertainties, with coefficients u_0 , u_1 , and u_2 that are estimated by comparison with reference
348 measurements at lower altitudes and the shot noise at higher altitude. The second term in Eq. 3, quadratic in r ,
349 reflects the quadratic rise of the noise of the unsmoothed quantities. We select the reference distance r_{ref} at the
350 upper end of the data evaluation range. By the approach with Eq. 3 considerable computation efforts have been
351 avoided. The results of the night-time series (Sect. 4.4) verify the approximation.

352 4. Results

353 4.1 UFS lidar results

354 The lidar test phase presented in Sects. 4.1 to 4.3 covers the 14 measurements made between November 2018
355 and February 2022. In addition, four separate night-time series are presented in Sect. 4.4.



356 In Fig. 3 we show the result of a revised data evaluation of the example shown by Klanner et al. (2021) based on
357 the slightly enhanced smoothing described in Sect. 3.1 and an exponential correction of the analogue profile that
358 was missing in the earlier evaluation. In addition, an aerosol correction was made that resulted in good
359 agreement with the temperature profile of the Munich radiosonde down to 12 km. The ripple below 32 km is a
360 result of the aerosol correction. Below 12 km the signal was partly cut off by rotating the laser beam to shift the
361 return bundle towards one side the entrance aperture of the detection system in order to limit the maximum
362 signal.

363 The GRIPS value was determined from an average of the GRIPS temperatures during the measurement period of
364 the lidar, which was done for all cases. The error bar represents the standard deviation for that period and does
365 not include the uncertainty due to the shifted horizontal position of the OH* layer south of the Central Alps. This
366 influences the results in an uncertainty of ± 5 K, sometimes more. The GRIPS value in this example agreed
367 sufficiently well with the lidar temperature generated by initiating the retrieval with the U.S. Standard
368 temperature at 88 km. Thus, the calibration was not shifted.

369 The NCEP data agree well with the radiosonde temperatures up to the operating range of the balloon. There is a
370 small deviation with respect to the lidar at 40 and 46 km. We do not know if this bias is caused by a vertical shift
371 of the NCEP profile.

372 We also added temperature profiles from MLS and the MOHp lidar. Unfortunately, no T profile from MOHp
373 was available for the same night, and we took the results from the two neighbouring measurement nights. The
374 average of both MOHp profiles agrees quite well with the UFS profile to about 70 km. The MLS profiles are
375 shown for about 13:31 CET (Central European Time, three thin orange lines) and about 3:05 CET on 17
376 November 2018 (three blue lines), named “noon” and “midnight”, respectively. The agreement should be better
377 for the “midnight” measurement, but the best agreement is limited to the spike region around 64 km. In principle,
378 this could be ascribed to the pronounced difference in longitude.

379 **4.1 Comparisons of the temperatures from the UFS lidar and the NCEP archive**

380 Up to the burst altitudes of the balloons (mostly 30 to 33 km) the temperature of the Munich radiosonde is nicely
381 reproduced. For higher altitudes the temperatures are compared for all NDACC stations from the NCEP data.
382 The NCEP profiles are listed up to roughly 55 km. Again, geopotential heights are converted to absolute heights.
383 Trickl et al. (2024) found for the evaluation of stratospheric aerosol that the Rayleigh reference profiles
384 calculated from the NCEP density and temperature data look highly reliable up to the chosen Klett (1983)
385 reference distance of 45 km (absolute altitude 47.675 km). However, the requirements for the temperature are
386 much higher. For the temperature data we found, in comparison with the UFS lidar, reasonable agreement up to
387 35 km, but sometimes deviations above this altitude (and below 50 km) of up to about 10 K occur (see Fig. 3 and
388 examples in the following sections; in one case even more). Sometimes there is the impression of a vertical shift
389 of the NCEP profile or a slightly wrong gradient in the range of the strongest temperature increase. The NCEP
390 profiles are calculated for noon UTC (13:00 CET) which certainly limits the comparability.

391 **4.2 Comparison the temperatures from the UFS lidar and MLS**

392 After initially concentrating just on the co-ordinates of the satellite for a given date (e.g., Klanner et al., 2021)
393 we now also looked at the times of the MLS overpasses, which resulted in a somewhat different view. The mean
394 passage times specified were 1.38 (± 0.40) h with respect to noon (CET) and 2.69 (± 0.39) h with respect to the



395 following midnight (CET). The “midnight” passages can be expected to be the better choice for the comparisons
396 with the early-night lidar measurements and were normally taken for the statistical evaluation. Morning times on
397 a given day were no longer used. For the downloaded data we consistently found the three latitudes 45.9° N,
398 47.35° N and 48.8° N which is sufficiently close to UFS (within $\pm 1.6^\circ$). By contrast, the longitudes were not
399 reproducible and ranged between 3.2° E and 20.7° E. For just two of the days the longitude perfectly matched
400 that of UFS. However, these profiles did not agree with those from the lidar significantly better. In two cases one
401 measurement time group of MLS was missing, and we took the profile for a passage at a time difference of about
402 ± 12 h with respect to midnight.

403 In addition to Fig. 3 we show in Fig. 4 six examples of comparisons. On average the positive bias of the
404 temperatures from the lidar and that from MLS remained. The best agreement below 70 km is seen in the
405 midnight comparisons (MLS: thin blue lines) in Fig. 3 and Fig. 4e. In three of the cases (not shown in Fig. 4) big
406 positive temperature peaks exceeding the estimated uncertainties could be seen above 70 km in the lidar data.
407 One of these cases is shown in Sect. 4.3. In addition, in Fig. 4f there is a rather excessive deviation between lidar
408 and MLS at 69 km, but here the temperature difference with respect to the MOHp lidar is smaller (thick blue
409 line). Because of the good latitudinal matching this discrepancy is strange. We are unable to explain it. One
410 could think either about wave effects or about an outlier of the lidar measurement. For identifying waves one
411 needs time series which is possible because of the one-hour time resolution of the system.

412 A very strange deviation was untypically found at rather low altitude for 12 December 2018 (not shown). At the
413 moderate altitude of 46 km the midnight MLS temperature was lower by as much as 25 K than that from the
414 lidar. The difference with respect to the MLS noon temperatures had been just 15 K, also this, however, being
415 out of any expectation for this altitude range. Below 35 km and above 57 km the agreement was reasonable to
416 excellent. For our statistical analysis (see below) we took the noon profile.

417 In Fig. 5 we show the differences of the profiles for all measurements, as well as the arithmetic average and the
418 positive and negative standard deviation. For the averages we selected the MLS latitude 47.35° N, -0.07° away
419 from that of UFS. In all but two cases the “midnight” MLS profile was taken. The maximum deviations for the
420 lidar are 9.4 K at 52.8 km and 8.6 K at 68.6 km. The minimum difference is found at 61.0 km is 3.1 K.

421 The negative temperature deviation of MLS confirms the findings in earlier work. Schwartz et al. (2008)
422 compared the MLS temperature profiles with those from several other satellite-borne sensors. They abruptly
423 started to depart from the other profiles above 45 km, the maximum negative offset reaching values between 5
424 and 8 K. The minimum difference around 60 km is also confirmed. Wing et al. (2018b; 2021) found a similar
425 behaviour for other Rayleigh lidar systems.

426 4.3 Comparisons of the temperatures from the UFS and MOHp lidar systems

427 Instead of comparing the UFS results with another satellite-borne sensor such as the proven SABER (Sounding
428 of the Atmosphere using Broadband Emission Radiometry; launch: December 2001; Russell et al., 1999;
429 Mertens et al., 2009; Esplin et al., 2023) we preferred to compare our temperature results with those of the
430 nearby MOHp ozone lidar. The advantage is the mentioned relatively small distance between the two lidar sites
431 The MOHp temperatures have been demonstrated to match the SABER temperatures almost perfectly (Fig. 10 of
432 Wing et al., 2021), as is the case also for other lidar stations (e.g., Cooper, 2004; Wing et al., 2018b; Dawkins et
433 al., 2018). Thus, we see the MOHp lidar as a suitable reference (see also Steinbrecht et al., 2025). During 8 of
434 the 14 measurement nights at UFS the MOHp lidar was operated as well.



435 As expected from earlier work (e.g., Wing et al., 2018b; 2021) the UFS and MOHp lidar temperature channels
436 yield a better agreement than the comparisons of the UFS lidar with MLS. However, the temperatures for the
437 two lidar sites may differ. In Fig. 6 the best case is presented with almost identical values up to 71 km (8
438 November 2021). Above this altitude the UFS temperature profile exhibits a pronounced peak strongly outside
439 the estimated uncertainty above this altitude. The MLS values sometimes deviate strongly which is associated
440 with bad temporal and spatial co-incidence.

441 The excellent agreement of the lidar results at both stations in Fig. 6 suggests that there is no fundamental
442 mismatch of the retrieval algorithms. Also in Fig. 7 the results do not differ much, except for the range above 66
443 km. There, the deviation is, still, within the expected uncertainty or the temperature variations suggested by the
444 variability in the GRIPS data. This agreement also suggests the absence of fluorescence effects of the
445 interference filters or PMT issues (see Sect. 5).

446 However, the examples in Fig. 4 demonstrate that there is, on average, a systematically lower temperature in the
447 MOHp values. This is somewhat surprising because of the good matching of the MOHp temperatures with
448 SABER (Wing et al., 2021) and a similar average offset between SABER and MLS (Schwartz et al., 2008) as
449 found for the UFS lidar in Fig. 5. At least, the agreement between the two lidar systems is clearly better than that
450 in Fig. 5.

451 This behaviour will be discussed in Sect. 5.

452 **4.4 Comparisons of night-time series at UFS with the MOHp all-night temperature profiles**

453 One issue of comparisons of the lidar measurements at UFS and MOHp is that the measurements at UFS are
454 confined to one hour and were, until 2022, concentrated to the first half of the night, whereas the soundings at
455 MOHP cover full nights. Although on average a night-time temperature increase has been found at the altitude of
456 the OH layer and ascribed to atmospheric tides we speculated on potential night-time cooling of the atmosphere
457 below. Of course, such an effect is difficult to evaluate in the presence of pronounced atmospheric wave
458 activities.

459 We, therefore, carried out four night-time series in November 2024, i.e., after the end of the period of
460 investigation in the previous sections (February 2022). The measurements were carried out with durations of just
461 half an hour, which resulted in a higher variability of the values at high altitudes than for the 1-h measurements.
462 Figure 8 shows the examples for the last two of the four nights, for which MOHp reference profiles existed and
463 for which the GRIPS temperature variability was low. During these nights the differences of the single-night
464 average UFS and the MOHp temperatures are rather small. Very few profiles depart strongly from the average,
465 beyond our expectations.

466 In Fig. 9 we present temperature time series of these two nights for altitudes differing by 5 km between 30 and
467 80 km. Up to 55 km the series are sufficiently smooth to allow us to judge temperature trends. There is no
468 indication of major night-time atmospheric cooling over a large altitude range, which is favourable for a good
469 agreement of the two lidar systems. The negative temperature development at 45 km and 50 km during the night
470 between 4 and 5 November could be an exception, but does not exceed the range of the temperature variability.
471 For the other two nights no cooling outside the temperature variability is observed (not shown).

472 Due to the enhanced noise of the half-hour sounding many lidar temperature profiles could not be evaluated to
473 clearly beyond 80 km. This made the calibration by using the GRIPS values impossible. Nevertheless, we used
474 estimates of the behaviour in the uppermost part of the measurements for a reasonable approach, also looking at
475 the MOHp profiles. Thus, the results above 70 km are somewhat influenced by the reference to GRIPS. As a



476 result of this and because of the smaller number of cases that can be averaged at the highest altitudes the
477 standard deviation diminishes beyond 80 km.

478 **5. Discussion and Conclusions**

479 Klanner et al. (2021) demonstrated that with a powerful XeCl laser and the large receiver Raman backscatter
480 signal accumulated within one hour from atmospheric water can be resolved to more than 25 km during night-
481 time, allowing us to retrieve useful H₂O mixing ratios to at least 20 km. In this study we examine the
482 performance of the Rayleigh temperature channel also for one-hour measurements.

483 The smoothed backscatter signals of the temperature channel can be discerned from the background up to more
484 than 90 km. Since this corresponds to a small fraction of one count per bin the smoothing must be strong and
485 currently limits the vertical resolution at high altitudes to 2.9 km (as defined in the 1999 VDI guideline). The
486 temperatures can be retrieved starting at several kilometres below this. The retrieval in the uppermost part of the
487 altitude range benefits from the simultaneous OH* measurements at UFS. In cases when the useful range of the
488 lidar ends below 86 km estimates from extrapolations are used.

489 The rather systematic positive offset of the lidar temperatures with respect to those from MLS between roughly
490 40 km and 70 km confirms the expectations from earlier work (Schwartz et al., 2008; Medvedeva et al., 2014;
491 Wing et al., 2018b; 2021). As mentioned, other satellite-borne sensors, in particular SABER, have shown an
492 excellent agreement with lidar temperature data above several stations including MOHp.

493 The agreement of the UFS lidar with the “off” wavelength channel of the MOHp DIAL is better, but on average
494 the UFS temperatures from roughly 45 km to 70 km also deviate positively. However, several profiles agree
495 really well which, together with the agreement below 45 km, suggests that there is no fundamental problem with
496 the retrieval algorithm.

497 A positive temperature offset means a smaller slope of the air density and, thus, slower decay of the lidar
498 backscatter signal. A slower decay of the backscatter signal would be typical of known technical artefacts that
499 will be discussed below. Since the UFS temperatures are higher than those of MOHp this could suggest that the
500 problems are more on the side of the UFS lidar.

501 Signal components exhibiting exponential decay are typical artefacts in lidar signal processing. For example,
502 slow fluorescence decay of optical components, in particular of interference filters, could yield slightly higher
503 temperatures above a certain threshold altitude. A threshold behaviour around an altitude of about 40 km is,
504 indeed, observed. However, because of the excellent agreement between the two lidar systems in several cases
505 we hesitate to assume the presence of fluorescence.

506 In addition, electronic artefacts must be considered. Wing et al. (2018a) attribute positive T biases above 70 km
507 to some extent to electronic cross talk or bursts of transient electronic signals and present a method to discard
508 bad profiles influenced by a shot-by-shot numerical analysis. Such an approach is helpful, but limited to low to
509 moderate laser repetition rates because of limits in computation speed. In any case, due to sufficient spatial
510 filtering in our receiver our far-field background count rate is of the order of 0.2 h⁻¹ bin⁻¹ which means
511 negligible interference of bursts. In fact, PMT testing with covered photocathode in the detection system verified
512 even the mostly complete absence of dark counts. The detection system is located far away from sources of
513 electromagnetic interference in a metallic tower outside the building.

514 Small exponential wings of the backscatter signal that could give rise to higher temperatures can be caused by
515 signal-induced nonlinearities of photomultiplier tubes (Bristow et al., 1996). Two effects must be considered,
516 signal-induced gain change due to overload of the final dynode stages and signal-induced emission of the



517 photocathode. The first type is avoided by limiting the signal, the second one seems to be suppressed in the PMT
518 model chosen to a high degree by kinetic-energy filtering (removal) of the artificial low-energy electrons.
519 Indeed, signal-induced nonlinearities have been found to be absent for the Hamamatsu R7400 detectors under
520 conservative operating conditions, in particular for photon counting (e.g., Trickl et al., 2020; 2024). Kreipl
521 (2006) determined the $1/e$ decay time of an overloaded R7400-03 cathode to less than 30 μ s, i.e., much shorter
522 than the decay time of the backscatter signal of our temperature measurements. These tests had been carried out
523 at a cathode illumination higher by almost two orders of magnitude. In summary, we can exclude signal-induced
524 nonlinearities as the reason of the positive temperature deviations.

525 There is one important difference between the lidar measurements at UFS and MOHp. The measurements at
526 UFS have taken place before midnight or around midnight the latest. At MOHp, with the exception of the
527 favourable case in Fig. 6, the data acquisition lasted all night, with measurements times up to more than 12 h
528 during the cold season. Atmospheric cooling during the second part of the night could serve as an explanation
529 the observed difference. The GRIPS measurements examined in this study do not reveal reproducible cooling in
530 the mesopause region with progressing night. The GRIPS temperatures tend to grow with time. At lower
531 altitudes (e.g.) the examples of Kopp et al. (2015) do not allow us to resolve a temperature change because of the
532 wave structure superimposed on the temperature profiles. At least our night-time measurement series in
533 November 2024 demonstrate in these cases that in the almost complete absence of atmospheric cooling the
534 temperature differences obtained at UFS and MOHp stay strongly below the variability of the 0.5-h UFS lidar
535 data.

536 A bias caused by misalignment can be excluded since this would lead to deviations at low altitudes. This kind of
537 problem has been limited to altitudes below 20 km.

538 Apart from these issues a range extension to more than 105 km is desirable since this would allow us to retrieve
539 temperatures with uncertainties of the order of ± 5 K up to almost 90 km, which covers the well-mixed part of the
540 atmosphere (U.S. Standard Atmosphere, 1976). The GRIPS measurement range would then be included in the
541 useful operating range of the lidar and the temperature obtained from the spectra could be controlled by vertical
542 sounding. As one can judge from Fig. 1 such a range extension would require a ten times higher laser power.
543 Since the pulse energy of the current laser is adequate for not exceeding signal levels that ensure linear detection
544 a much higher pulse repetition rate would be the solution. Diode-laser-pumped Nd:YAG with similar third-
545 harmonic pulse energies but a repetition rate of more than 300 Hz are meanwhile commercially available. 300
546 Hz would match the repetition rate of the XeCl laser and water vapour and temperature measurements could be
547 made simultaneously, with delayed pulses in order to minimize spectral interference. This would mean 15 times
548 the power of the current transmitter.

549 In three cases we observed excessive temperature peaks around and above 70 km. Because of the low signal
550 level at these altitudes we cannot exclude signal outliers which, again, calls for a higher backscatter signal.
551 However, temperature excursions of the order of 20 K in the mesopause region have been presented in earlier
552 work and attributed to waves (e.g., Kopp et al., 2015). A clear identification of gravity waves requires to carry
553 out our time series with a better signal-to-noise ratio.

554 In addition, an influence of particles or fluorescence from meteorites must be distinguished. One example of a
555 potential particle layer observed at 54 km with our stratospheric aerosol lidar (Trickl et al., 2013; 2024) is given
556 in Fig. 10. An identification of the presence of particles cannot be achieved with a simple backscatter lidar. The
557 particle contribution can be removed by spectral filtering the scattered light from a narrowband frequency-
558 doubled Nd:YAG laser in iodine (Piironen and Eloranta et al., 1994). For our system we could think of



559 additional measurements at the also available 532.2-nm laser emission with an iodine filter as successfully
560 implemented in our mobile aerosol lidar before (Giehl and Trickl, 2010; Wandinger et al., 2016). The problem of
561 the light absorption in ozone at 532.2 nm does not matter at high altitudes.
562 The advantage of symbiotic use of the GRIPS observations at UFS could be strengthened by adding a vertically
563 pointing spectrometer. In the near future, the current set-up with two identical spectrometers will be extended by
564 a third spectrometer that will be aligned for parallel measurements with the laser beam. This, together with less
565 noisy lidar data, would simplify the interpretation of remaining differences. More detailed studies of the airglow
566 layer could be made by tuning the fundamental wavelength of the Raman lidar wavelength to 308.15 nm where
567 OH laser-induced fluorescence can be excited (Brinksma et al., 1998).
568 After the completion of the upgrading the beginning of routine lidar measurements is planned, as a potential
569 contribution to NDACC.

570 **5 Data availability**

571 Lidar data from the UFS lidar can be obtained from the authors, but are currently flagged as preliminary. GRIPS
572 temperatures are available at <https://zenodo.org/records/15267440>. MLS v5 temperature data are available at
573 https://disc.gsfc.nasa.gov/datasets?page=1&keywords=ML2T_005/. A full list of MLS data can be found at
574 <http://disc.sci.gsfc.nasa.gov/Aura/dataholdings/>. The MOHp lidar data can be freely downloaded from the
575 NDACC data base (<https://www-air.larc.nasa.gov/missions/ndacc/data.html>).

576 **6 Author statement**

577 TT and HV carried out and evaluated the UFS lidar measurements. MB, CS and SW are responsible for the
578 GRIPS observations, WS for the lidar measurements at MOHp. GN preselected and provided the MLS data. All
579 authors contributed to preparing this manuscript.

580 **7 Competing interests**

581 The authors declare that they have no conflict of interest.

582 **Acknowledgements**

583 The authors from IMK-IFU thank Hans Peter Schmid for his support. Lisa Klanner (until 2015) and Matthias
584 Perfahl strongly contributed to the technical development of the system that recently has included remote
585 control. We are indebted to the considerable assistance of the UFS staff. The lidar development was funded by
586 the Bavarian Staatsministerium für Umwelt und Verbraucherschutz (BayStMUV). The GRIPS observations at
587 UFS have also been supported by BayStMUV in projects including GUDRUN, grant no. 71b-U8729-2003/125-
588 13; GRIPS3 Back-Up, 2009/40051; BHEA, TLK01U-49580; LUDWIG, TUS01UFS-67093; VoCaS,
589 TKP01KPB-70581; and AlpEn-DAC, TUS01UFS-72184). Gerald Nedoluha was supported by the NASA Earth
590 Sciences Division Upper Atmosphere Research Program and by the Office of Naval Research.

591
592 The service charges for this open access publication have been covered by a Research Centre of the Helmholtz
593 Association.

594 **References**



- 595 Alpers, M., Eixmann, R., Fricke-Begemann, C., Gerding, M., and Höffner, J.: Temperature lidar measurements
596 from 1 to 105 km altitude using resonance, Rayleigh, and Rotational Raman Scattering. *Atmos. Chem. Phys.*,
597 4,793–800, 2004.
- 598 Arnold, K. S., and She, C. Y.: Metal fluorescence lidar (light detection and ranging) and the middle atmosphere,
599 *Contemp. Phys.*, 44, 35 – 49, 2003.
- 600 Arshinov, Y. F., Bobrovnikov, S. M., Zuev, V. E., and Mitev, V. M.: Atmospheric temperature measurements
601 using a pure rotational Raman lidar, *Appl. Optics*, 22, 2984–2990, 1983.
- 602 Baker, D. J. and Stair, A. T.: Rocket measurements of the altitude distributions of the hydroxyl airglow, *Physica*
603 *Scripta*, 37, 611–622, <https://doi.org/10.1088/0031-8949/37/4/021>, 1988.
- 604 Behrendt, A.: Temperature Measurements with Lidar, pp. 273-305 in: *Lidar – Range-Resolved Optical Remote*
605 *Sensing of the Atmosphere*, Claus Weitkamp, Ed., Springer Science and Business Media (New York, U.S.A.),
606 ISBN 0-387-40075-3, 2005.
- 607 Beig, G., Keckhut, P., Lowe, R. P., Roble, R. G., Mlyneczak, M. G., Scheer, J., Fomichev, V. I., Offermann, D.,
608 French, W. J. R., Shepherd, M. G., Semenov, A. I., Remsberg, E. E., She, C. Y., Lübken, F. J., Bremer, J.,
609 Climesha, B. R., Stegman, J., Sigernes, F., and Fadnavis, S.: Review of mesospheric temperature trends, *Rev.*
610 *Geophys.*, 41, RG1015, <https://doi.org/10.1029/2002RG000121>, 2003.
- 611 Bittner, M., Offermann, D., and Graef, H. H.: Mesopause temperature variability above a midlatitude station in
612 Europe, *J. Geophys. Res.*, 105, 2045-2058, 2000.
- 613 M. Bittner, M., Offermann, D., Graef, H.-H., Donner, M., and Hamilton, K.: An 18-year time series of OH
614 rotational temperatures and middle atmosphere decadal variations, *J. Atmos. Solar-Terr. Phys.*, 64, 1147–1166,
615 2002.
- 616 Blamont, J. E., Chanin, M. L., and Mégie, G.: Vertical distribution and temperature profile of night time sodium
617 layer obtained by laser backscatter, *Ann. Geophys.*, 26, 833-838, 1972.
- 618 Bowman, M. R., Gibson, A. J., and Sandford, M. C. W.: Atmospheric Sodium measured by a Tuned Laser
619 Radar, *Nature*, 221, 456-457, 1969.
- 620 Brinksma, E. J., Meijer, Y. J., McDermid, I. S., Cageao, R. P., Bergwerf, J. B., Swart, D. P. J., Ubachs, W.,
621 Matthews, W. A., Hogervorst, W., and Hovenier, J. W.: First lidar observations of mesospheric hydroxyl,
622 *Geophys. Res. Lett.*, 25, 51-54, 1998; erratum: *Geophys. Res. Lett.*, 25, 521, 1998.
- 623 Bristow, M. P., Bundy, D. H., and Wright, A. G.: Signal linearity, gain stability, and gating in photomultipliers:
624 application to differential absorption lidars, *Appl. Opt.*, 34, 4437-4452, 1996.
- 625 Carnuth, W., Kempfer, U., and Trickl, T.: Highlights of the tropospheric lidar studies at IFU within the TOR
626 project, *Tellus B*, 54, 163-185, 2002.
- 627 Chen, H., White, M. A., Krueger, D. A., and She, C. Y.: Daytime mesopause temperature measurements with a
628 sodium-vapor dispersive Faraday filter in a lidar receiver, *Opt. Lett.*, 21, 1093-1095, 1996.
- 629 Chu, X., Gardner, C. S., and Papen, G.: Lidar Observations of Polar Mesospheric Clouds at South Pole: Diurnal
630 Variations, *Geophys. Res. Lett.*, 28, 1937-1940, 2001.



- 631 Cooper, M.: Validation of SABER Temperature Measurements Using Ground-based Instruments, IGARSS
632 2004. 2004 IEEE International Geoscience and Remote Sensing Symposium, IEEE Xplore,
633 <https://doi.org/10.1109/IGARSS.2004.1370033>, 2004.
- 634 Curtis, R. D., Houghton, J. T., Peskett, G. D., and Rodgers, C. D.: The pressure modulator radiometer for
635 Nimbus F, Proc. R. Soc. London, A 337, 135-150, 1974.
- 636 Dawkins, E. C. M., Feofilov, A., Rezac, L., Kutepov, A. A., Janches, D., Höffner, J., Chu, X., Lu, X., Mlynchak,
637 M. G., and Russell, J. III: Validation of SABER v2.0 operational temperature data with ground-based lidars in
638 the mesosphere-lower thermosphere region (75–105 km). *J. Geophys. Res.*, 123, 9916–9934, 2018.
- 639 Englert, C. R., Stevens, M. H., Siskind, D.-E., Harlander, J. M., and Roesler, F. L.: Spatial Heterodyne Imager
640 for Mesospheric Radicals on STPSat-1, *J. Geophys. Res.*, 115, D20306, doi:10.1029/2010JD014398, 20 pp.,
641 2010.
- 642 Esplin, R., Mlynchak, M. G., Russell, J., Gordley, L., and The SABER Team: Sounding of the Atmosphere using
643 Broadband Emission Radiometry (SABER): Instrument and Science Measurement Description, *Earth and Space*
644 *Science*, 10, e2023EA002999, 32 pp., 2023.
- 645 Fishbein, E. F., Cofield, R. E., Froidevaud, L., Jarnot, R. F., Lungu, I. T., Read, W. G., Shippony, Z., Waters, J.
646 W., McDermid, I. S., McGee, T. J., Singh, U., Gross, M., Hauchecorne, A., Keckhut, P., Gelman, M. E., and
647 Nagatani, R. M.: Validation of UARS Microwave Limb Sounder temperature and pressure measurements, *J.*
648 *Geophys. Res.*, 101, 9983-10016, 1996; the paper includes 353-nm measurements of the Table Mountain Facility
649 (McDermid et al., 1990).
- 650 Fricke, K. H., and von Zahn, U.: Mesopause temperatures derived from probing the hyperfine structure of the D₂
651 resonance line of sodium by lidar, *J. Atmos. Terr. Phys.*, 47, 499-512, 1985.
- 652 Gerding, M., Höffner, J., Kopp, M., Eixmann, R., and Lübken, F.-J.: Mesospheric temperature and aerosol
653 soundings during day and night: spectra land spatial filtering techniques. in: 25th International Laser Radar
654 Conference, St. Petersburg, Russia, 2010, pp. 67–70, 2010.
- 655 Giehl, H., and Trickl, T.: Testing the IFU High-Spectral-Resolution Lidar at the 2009 Leipzig Field Campaign,
656 pp. 920-923 in: Proceedings of the 25th International Laser Radar Conference, St.-Petersburg (Russia), July 5 to
657 9, 2010, G. Matvienko, A. Zemlyanov, Eds., V. E. Zuev Institute of Optics (Tomsk, Russia), 2010.
- 658 Gille, S. T., Hauchecorne, A., and Chanin, M.-L.: Semidiurnal and diurnal tidal effects in the middle atmosphere
659 as seen by Rayleigh lidar, *J. Geophys. Res.*, 96, 7579-7587, 1991.
- 660 Granier, C., Jegou, J. P., and Mégie, G.: Iron Atoms and Metallic Species in the Earth's upper Atmosphere,
661 *Geophys. Res. Lett.*, 16, 243-246, 1989.
- 662 Hannawald, P., Schmidt, C., Sedlak, R., Wüst, S., and Bittner, M.: Seasonal and intra-diurnal variability of
663 small-scale gravity waves in OH airglow at two Alpine stations, *Atmos. Meas. Tech.*, 12, 457–469, 2019
- 664 Hauchecorne, A., and Chanin, M.-L.: Density and Temperature Profiles Obtained by Lidar between 33 and 70
665 km, *Geophys. Res. Lett.*, 7, 565-568, 1980.
- 666 Hauchecorne, A., Chanin, M.-L., and Keckhut, P.: Climatology and Trends of the Middle Atmospheric
667 Temperature (33–87 km) as Seen by Rayleigh Lidar over the South of France, *J. Geophys. Res.*, 96, 15297-
668 15309, 1991.



- 669 Höffner, J., and Lautenbach, J.: Daylight measurements of mesopause temperature and vertical wind with the
670 mobile scanning iron lidar, *Opt. Lett.* 34, 1351-1353 (2009)
- 671 Höveler, K.: Entwicklung eines Nahbereichsempfängers zur Messung von Wasserdampf- und Temperaturpro-
672 filen für das Hochleistungs-Raman-Lidar am Schneefernerhaus, Masterarbeit, Karlsruher Institut für
673 Technologie, Fakultät für Physik, 138 pp., 2015 (in German).
- 674 Iarlori, M., Madonna, F., Rizi, V., Trickl, T., and Amodeo, A.: Effective resolution concepts for lidar
675 observations, *Atmos. Meas. Tech.*, 8, 5157–5176, <https://doi.org/10.5194/amt-8-5157-2015>, 2015.
- 676 Jäger, H. and Deshler, T.: Lidar backscatter to extinction, mass and area conversions for stratospheric aerosols
677 based on midlatitude, *Geophys. Res. Lett.*, 29, 1929, 2002.
- 678 Jäger, H. and Deshler, T.: Correction to “Lidar backscatter to extinction, mass and area conversions for
679 stratospheric aerosols based on midlatitude balloonborne size distribution measurements”, *Geophys. Res. Lett.*,
680 30, 1382, 2003.
- 681 Keckhut, P.: Middle atmospheric temperature measurements with lidar, *J. Physique*, 121, 239–248, 2004.
- 682 Khanna, J., Bandoro, J., Sica, R. J., and McElroy, C. T.: New technique for retrieval of atmospheric temperature
683 profiles from Rayleigh-scatter lidar measurements using nonlinear inversion, *Appl. Opt.*, 51, 7945-7852, 2012.
- 684 Kim, Y.-J., Eckermann, S. D., and Chun, H.-Y.: An overview of the past, present and future of gravity wave
685 drag parametrization for numerical climate and weather prediction models. *Atmosphere-Ocean*, 41, 65-98, 2003.
- 686 Klanner, L.: Entwicklung eines Hochleistungs-Raman-Lidars für die Messung von Wasserdampf- und
687 Temperaturprofilen in der Atmosphäre, Technische Universität München, Fakultät Wissenschaftszentrum
688 Weihenstephan, Dissertation, 186 pp., 2022 (in German).
- 689 Klanner, L., Höveler, K., Khordakova, D., Perfahl, M., Rolf, C., Trickl, T., and Vogelmann, H.: A powerful lidar
690 system capable of 1 h measurements of water vapour in the troposphere and the lower stratosphere as well as the
691 temperature in the upper stratosphere and mesosphere, *Atmos. Meas. Tech.*, 14, 531-555, 2021.
- 692 Klett, J. D.: Stable analytical inversion solution for processing lidar returns, *Appl. Opt.*, 20, 211-220, 1981.
- 693 Klett, J. D.: Lidar inversion with variable backscatter/extinction ratios, *Appl. Opt.*, 24, 1638-1643, 1985.
- 694 Kopp, M., Gerding, M., Höffner, J., and Lübken, F.-J.: Tidal signatures in temperatures derived from daylight
695 lidar soundings above Kühlungsborn (54°N, 12°E), *J. Atmos. Sol.-Terr. Phys.*, 127, 37–50, 2015.
- 696 Kreipl, S.: Messung des Aerosoltransports am Alpennordrand mittels Laserradar (Lidar), Dissertation, Friedrich-
697 Alexander-Universität Erlangen-Nürnberg (Germany), 195 pp., 2006 (in German); the relevant figure can be
698 found at <http://www.trickl.de/PMT.PDF>.
- 699 Leblanc, T., McDermid, I. S., Keckhut, P., Hauchecorne, A., She, C. Y., and Krueger, D. A.: Temperature
700 climatology of the middle atmosphere from long-term lidar measurements at middle and low latitudes, *J.*
701 *Geophys. Res.*, 103, 17191-17204, 1998
- 702 Leblanc, T., Sica, R. J., van Gijzel, J. A. E., Godin-Beekmann, S., Haefele, A., Trickl, T., Payen, G., and
703 Gabarrot, F.: Proposed standardized definitions for vertical resolution and uncertainty in the NDACC lidar ozone
704 and temperature algorithms – Part 1: Vertical resolution, *Atmos. Meas. Tech.*, 9, 4029–4049,
705 <https://doi.org/10.5194/amt-9-4029-2016>, 2016.6.



- 706 Liu, G. and Shepherd, G. G.: An empirical model for the altitude of the OH nightglow emission, *Geophys. Res.*
707 *Let.*, 33, L09805, <https://doi.org/10.1029/2005gl025297>, 2006.
- 708 Li, A., Roth, C. Z., Bourassa, A. E., Degenstein, D. A., Pérot, K., Christensen, O. M., and Murtagh, D. P.: The
709 OH (3-1) nightglow volume emission rate retrieved from OSIRIS measurements: 2001 to 2015. *Earth Syst. Sci.*
710 *Data*, 13(11), 5115-5126, <https://doi.org/10.5194/essd-13-5115-2021>, 2021.
- 711 Lopez-Moreno, J. J., Rodrigo, R., Moreno, F., Lopez-Puertas, M., and Molina, A.: Altitude distribution of
712 vibrationally excited states of atmospheric hydroxyl at levels $v = 2$ to $v = 7$, *Planet. and Space Sci.*, 35(8), 1029-
713 1038, [https://doi.org/10.1016/0032-0633\(87\)90007-9](https://doi.org/10.1016/0032-0633(87)90007-9), 1987.
- 714 McDermid, I. S., Godin, S. M., and Walsh, T. D.: Lidar measurements of stratospheric ozone and
715 intercomparisons and validation, *Appl. Opt.*, 29, 4914-4923, 1990.
- 716 Medvedev, A. S., and Yiğit, E.: Gravity waves in planetary atmospheres: Their effects and parameterization in
717 global circulation models. *Atmosphere*, 10, 531, 2019.
- 718 Medvedewa, I. V., Semenov, A. I., Perminov, V. I., Beletsky, A. B., and Tartarnikov, A. V.: Comparison of
719 Ground-based OH Temperature Data Measured at Irkutsk (52°N, 103°E) and Zvenigorod (56°N, 37°E) Stations
720 with Aura MLS v3.3, 62, pp. 340-349, DOI: 10.2478/s11600-013-0161-x, 2014.
- 721 Mégie, G., Bos, F., Blamont, J. E., and Chanin, M. L.: Simultaneous Nighttime Measurements of Sodium and
722 Potassium, *Planet. Space Sci.*, 26, 27-35, 1978.
- 723 Mertens, C. J., Russell, J. M. III, Mlynczak, M. G., She, C.-Y., Schmidlin, F. J., Richard A. Goldberg, R. A.,
724 López-Puertas, M., Wintersteiner, P. P., Picard, R. H., Winick, J. R., and Xu, X.: Kinetic temperature and carbon
725 dioxide from broadband infrared limb emission measurements taken from the TIMED/SABER instrument, *Adv.*
726 *Space Res.*, 43, 15–27, 2009.
- 727 Mulligan, F., Horgan, D., Galligan, J., and Griffin, E.: Mesopause temperatures and integrated band brightnesses
728 calculated from airglow OH emissions recorded at Maynooth (53.2° N, 6.4° W) during 1993, *J. Atmos. Terr.*
729 *Phys.*, 57, 1623–1637, 1995.
- 730 Mohr, P. J., Newell, D. B., and Taylor, B. N.: CODATA recommended values of the fundamental physical
731 constants: 2014, *Rev. Modern Phys.*, 88, 035009, 73 pp., 2016.
- 732 Nedoluha, G. E. , Gomez, R. M., Boyd, I. , Neal, H., Allen, D. R., and Lambert, A.: The Spread of the Hunga
733 Tonga H₂O Plume in the Middle Atmosphere Over the First Two Years Since Eruption, *J. Geophys. Res.*, 129,
734 e2024JD040907. <https://doi.org/10.1029/2024JD0409>, 11 pp., 2024.
- 735 Nedoluha, G. E. , Gomez, R. M., Boyd, I. , Neal, H., Allen, D. R., Parrish, A., Connor, B.- J., and Siskind, D. E.:
736 Measurements of Stratospheric ClO From Mauna Kea: 1992–2023, *J. Geophys. Res.*, 130, e2024JD041848.
737 <https://doi.org/10.1029/2024JD041848>, 13 pp., 2025.
- 738 Noll, S., Kimeswenger, S., Proxauf, B., Unterguggenberger, S., Kausch, W., and Jones, A. M.: 15 years of
739 VLT/UVES OH intensities and temperatures in comparison with TIMED/SABER data, *J. Atmos. Sol.-Terr.*
740 *Phys.*, 163, 54–69, 2017.
- 741 Noll, S., Winkler, H., Goussev, O., and Proxauf, B.: OH level populations and accuracies of Einstein-A
742 coefficients from hundreds of measured lines, *Atmos. Chem. Phys.*, 20, 5269–5292, 2020.
- 743 Noll, S., Schmidt, C., Kausch, W., Bittner, M., and Kimeswenger, S.: Climatologies of various OH lines from
744 about 90,000 X-shooter spectra, *J. Geophys. Res.*, 128, <https://doi.org/10.1029/2022JD038275>, 2023.



- 745 Ott, H.: Single atom detection in ultracold quantum gases: a review of current progress, *Rep. Prog. Phys.*, 79,
746 054401, 2016.
- 747 Papen, G. C., Pfenninger, W. M., and Simonich, D. M.: Sensitivity analysis of Na narrowband wind-temperature
748 lidar systems, *Appl. Opt.*, 34, 480-498, 1995.
- 749 Piironen, P., and Eloranta, E. W.: Demonstration of a high-spectral-resolution lidar based on an iodine
750 absorption filter, *Opt. Lett.*, 19, 234-236, 1994.
- 751 Reisin, E. R., Scheer, J., Dyrland, M. E., Sigernes, F., Deehr, C. S., Schmidt, C., Höppner, K., Bittner, M.,
752 Ammosov, P. P., Gavrilieva, G. A., Stegman, J., Perminov, V. I., Semenov, A. I., Knieling, P., Koppmann, R.,
753 Shiokawa, K., Lowe, R. P., López-González, M. J., Rodríguez, E., Zhao, Y., Taylor, M. J., Buriti, R. A., Espy, P.
754 J., French, W. J. R., Eichmann, K.-U., Burrows, J. P., and von Savigny, C.: Traveling planetary wave activity
755 from mesopause region airglow temperatures determined by the Network for the Detection of Mesospheric
756 Change (NDMC), *J. Atmos. Sol.-Terr. Phys.*, 119, 71–82, 2014.
- 757 Russell, J. M. III, Mlynczak, M. G., Gordley, L. L., Tansock, J., and Esplin, R.: An overview of the SABER
758 experiment and preliminary calibration results, *Proc. SPIE*, 3756, 277-288, 1999.
- 759 Scheer, J., Reisin, E. R., Espy, J. P., Bittner, M., Graef, H. H., Offermann, D., Ammoso, P. P., and Ignatyev, V.
760 M.: Large-scale structures in hydroxyl rotational temperatures during DYANA, *J. Atmos. Terr. Phys.*, 56, 1701-
761 1715, 1994.
- 762 Schmidt, C., Höppner, K., and Bittner, M.: A ground-based spectrometer equipped with an InGaAs array for
763 routine observations of OH (3-1) rotational temperatures in the mesopause region, *J. Atmos. Sol.-Terr. Phys.*,
764 102, 125–139 2013.
- 765 Schmidt, C., Dunker, T., Lichtenstern, S., Scheer, J., Wüst, S., Hoppe, U.-P., and Bittner M.: Derivation of
766 vertical wavelengths of gravity waves in the MLT-region from multispectral airglow observations, *J. Atmos.*
767 *Sol.-Terr. Phys.*, 173, 119-127, <https://doi.org/10.1016/j.jastp.2018.03.002>, 2018.
- 768 Schmidt, C., Küchelbacher, L., Wüst, S., and Bittner, M.: OH airglow observations with two identical
769 spectrometers: benefits of increased data homogeneity in the identification of variations induced by the 11-year
770 solar cycle, the QBO, and other factors. *Atmos. Meas. Tech.* 16, 4331-4356, [https://doi.org/10.5194/amt-16-](https://doi.org/10.5194/amt-16-4331-2023)
771 4331-2023, 2023.
- 772 Schoeberl, M. R., Douglass, A. R., Hilsenrath, E., Bhartia, P. K., Beer, R., Waters, J. W., Gunson, M. R.,
773 Froidevaux, L., Gille, J. C., Barnett, J. J., Levelt, P. F., and DeCola, P.: Overview of the EOS Aura mission,
774 *IEEE Trans. Geosci. Remote Sens.*, 44, 1066–1074, 2006.
- 775 Schwartz, M. L., Lambert, A., Manney, G. L., Read, W. G., Livesey, N. E., J., Froidevaux, L., Ao, C. O.,
776 Bernath, P. F., Boone, C. D., Cofield, R. E., Daffer, W. H., Drouin, B. J., Fetzer, E. J., Fuller, R. A., Jarnot, R.
777 F., Jiang, J. H., Jiang, Y. B., Knosp, B. W., Krüger, K., Li, J.-L. F., Mlynczak, M. G., Pawson, S., Russell, J. M.
778 III, Santee, M. L., Snyder, W. V., Stek, P. C., Thurstans, R. P., Tompkins, A. M., Wagner, P. A., Walker, K. A.,
779 Waters, J. W., and Wu, D. L.: Validation of the Aura Microwave Limb Sounder temperature and geopotential
780 height measurements, *J. Geophys. Res.*, 113, D15S11, doi: 10.1029/2007JD008783, 23 pp., 2008.
- 781 Serikov, I., and Bobrinikov, S.: Atmospheric temperature profiling with pure rotational Raman lidars, pp. 149-
782 216, Series: Optoelectronic Materials and Devices, Vol. 7, Recent Advances in Atmospheric Lidars, L. Fiorani,



- 783 and V. Mitev, Eds., National Institute of Research and Development for Optoelectronics (Bucharest, Romania),
784 ISBN 978-973-88109-6-9, 2009.
- 785 She, C. Y., and Lowe, R.P.: Seasonal temperature variations in the mesopause region at mid-latitudes:
786 Comparison of lidar and hydroxyl rotational temperatures using WINDII/UARS OH height profiles, *J. Atmos.*
787 *Solar-Terr. Phys.*, 60, 1573–1583, 1998.
- 788 She, C. V., Lativi, H., Yu, Y. R., Alvarez II, R. J., Bills, R. E., and Gardner, C. S.: Two-frequency Lidar
789 Technique for Mesospheric Na Temperature Measurements, *Geophys. Res. Lett.*, 17, 929-932, 1990.
- 790 Shibata, T., Kobuchi, M., and Maeda, M.: Measurements of density and temperature profiles in the middle
791 atmosphere with a XeF lidar, *Appl. Optics*, 25, 685–688, 1986.
- 792 Sica, R. J., Measurements of the Effects of Gravity Waves in the Middle Atmosphere Using Parametric Models
793 of Density Fluctuations. Part II: Energy Dissipation and Eddy Diffusion, *J. Atmos. Sci.*, 56, 1330-1343, 1999.
- 794 Sica, R. J., Sargoytchev, S., Argall, P. S., Borra, E. F., Girard, L., Sparrow, C. T., and Flatt, S.: Lidar
795 measurements taken with a large-aperture liquid mirror. 1. Rayleigh-scatter system, *Appl. Opt.*, 34, 6925-6936,
796 1995.
- 797 Sivjee, G. G.: Airglow Hydroxyl Emissions, *Planet. Space Sci.*, 40, 235–242, 1992.
- 798 Steinbrecht, W., Velasco, V. A., Dirksen, R., Doppler, L., Oelsner, P., Van Malderen, R., De Backer, H.,
799 Maillard Barras, E., Stübi, R., Godin-Beekmann, S., and Hauchecorne, A.: Ground-Based Monitoring of
800 Stratospheric Ozone and Temperature Over Germany Since the 1960s, *Earth Space Sci.*, 12, e2024EA003821, 24
801 pp., <https://doi.org/10.1029/2024>, 2025.
- 802 Takahashi, H., Clemesha, B. R., Simonich, D. M., Melo, S. M. L., Teixeira, N. R., Eras, A., Stegman, J., Witt,
803 G.: Rocket measurements of the equatorial airglow: MULTIPHOT 92 database, *J. Atmos. Terr. Phys.*, 58, 1943–
804 1961, 1996.
- 805 Trickl, T.: Upgraded 1.56- μ m lidar at IMK-IFU with 0.28 J/pulse, *Appl. Opt.*, 49, 3732-3740, 2010.
- 806 Trickl, T., Giehl, H., Jäger, H., and Vogelmann, H.: 35 years of stratospheric aerosol measurements at Garmisch-
807 Partenkirchen: from Fuego to Eyjafjallajökull, and beyond, *Atmos. Chem. Phys.*, 13, 5205-5225, 2013.
- 808 Trickl, T., Vogelmann, H., Giehl, H., Scheel, H. E., Sprenger, M., and Stohl, A.: How stratospheric are deep
809 stratospheric intrusions? *Atmos. Chem. Phys.*, 14, 9941-9961, 2014.
- 810 Trickl, T., Vogelmann, H., Flentje, H., and Ries, L.: Stratospheric ozone in boreal fire plumes – the 2013 smoke
811 season over Central Europe, *Atmos. Chem. Phys.*, 15, 9631-9649, 2015.
- 812 Trickl, T., Vogelmann, H., Fix, A., Schäfler, A., Wirth, M., Calpini, B., Levrat, G., Romanens, G., Apituley, A.,
813 Wilson, K. M., Begbie, R., Reichardt, J., Vömel, H. and Sprenger, M.: How stratospheric are deep stratospheric
814 intrusions into the troposphere? LUAMI 2008, *Atmos. Chem. Phys.*, 16, 8791-8815, 2016.
- 815 Trickl, T., Neidl, F., Giehl, H., Perfahl, M., and Vogelmann, H.: Three decades of tropospheric ozone lidar
816 development at Garmisch-Partenkirchen, *Atmos. Meas. Tech.*, 13, 6357-6390, 2020.
- 817 Trickl, T., Adelwart, M., Khordakova, D., Ries, L., Rolf, C., Steinbrecht, W., and Vogelmann, H.: Local
818 comparisons of tropospheric ozone: Vertical sounding at two neighbouring stations in Southern Bavaria, *Atmos.*
819 *Meas. Tech.*, 16, 5145–5165, 2023.



- 820 Trickl, T., Vogelmann, H., Fromm, M. F., Jäger, H., Perfahl, M., and Steinbrecht, W.: Measurements report:
821 Violent biomass burning and volcanic eruptions: a new period of elevated stratospheric aerosol over Central
822 Europe (2017 to 2023) in a long series of observations, *Atmos. Chem. Phys.*, 24, 1997–2021, 2024.
- 823 U.S. Standard Atmosphere: National Oceanic and Atmospheric Organization (NOAA), National Aeronautics and
824 Space Administration, United States Air Force, NOAA-S/T 76-1562, US Printing Office (Washington, D.C.),
825 227 pp., 1976.
- 826 VDI: guide line 4210 Remote Sensing, Atmospheric Measurements with LIDAR, Measuring gaseous air
827 pollution with the DAS LIDAR, Verein Deutscher Ingenieure, Düsseldorf, Germany, 47 pp., 1999.
- 828 Vogelmann, H. and Trickl, T.: Wide-Range Sounding of Free-Tropospheric Water Vapor with a Differential-
829 Absorption Lidar (DIAL) at a High-Altitude Station, *Appl. Opt.*, 47, 2116–2132, 2008.
- 830 Vogelmann, H., Sussmann, R., Trickl, T., and Borsdorff, T.: Intercomparison of atmospheric water vapor
831 soundings from the differential absorption lidar (DIAL) and the solar FTIR system on Mt. Zugspitze, *Atmos.*
832 *Meas. Tech.*, 4, 835–841, 2011.
- 833 Von Savigny, C., McDade, I. C., Eichmann, K.-U., and Burrows, J. P.: On the dependence of the OH* Meinel
834 emission altitude on vibrational level: SCIAMACHY observations and model simulations, *Atmos. Chem. Phys.*,
835 12, 8813–8828, 2012.
- 836 Von Savigny, C. and Lednyts'kyi, O.: On the relationship between atomic oxygen and vertical shifts between
837 OH Meinel bands originating from different vibrational levels, *Geophys. Res. Lett.* 40, 5821–5825.
838 <https://doi.org/10.1002/2013GL058017>, 2013.
- 839 Von Zahn, U., Fricke, K. H., Gerndt, R., and Blix, T.: Mesospheric temperatures and the OH layer height as
840 derived from ground-based lidar and OH* spectrometry, *J. Atmos. Terr. Phys.*, 38, 49, 863–869, 1987.
- 841 Von Zahn, U., von Cossart, G., Fiedler, J., Fricke, K. H., Nelke, G., Baumgarten, G., Rees, D., Hauchecorne, A.,
842 and Adolfsen, K.: The ALOMAR Rayleigh/Mie/Raman lidar: objectives, configuration, and performance, *Ann.*
843 *Geophysicae*, 18, 815–833, 2000.
- 844 Waters, J. W., Froidevaux, L., Harwood, R. S., Jarnot, R. F., Pickett, H. M., Read, W. G., Siegel, P. H., Cofield,
845 R. E., Filipiak, M. J., Flower, D. A., Holden, J. R., Lau, G. K., Livesey, N. J., Manney, G. L., Pumphrey, H. C.,
846 Santee, M. L., Wu, D. L., Cuddy, D. T., Lay, R. R., Loo, M. S., Perun, V. S., Schwartz, M. J., Stek, P. C.,
847 Thurstans, R. P., Boyles, M. A., Chandra, K. M., Chavez, M. C., Chen, G.-S., Chudasama, B. V., Dodge, R.,
848 Fuller, R. A., Girard, M. A., Jiang, J. H., Jiang, Y., Knosp, B. W., LaBelle, R. C., Lam, J. C., Lee, K. A., Miller,
849 D., Oswald, J. E., Patel, N. C., Pukala, D. M., Quintero, O., Scaff, D. M., Van Snyder, W., Tope, M. C., Wagner,
850 P. A., and Walch M. J.: The Earth Observing System Microwave Limb Sounder (EOS MLS) on the Aura
851 satellite, *IEEE Trans. Geosci. Remote Sens.*, 44, 1075–1092, 2006.
- 852 Wandinger, U., Freudenthaler, V., Baars, H., Amodeo, A., Engelmann, R., Mattis, I., Groß, S., Pappalardo, G.,
853 Giunta, A., D'Amico, G., Chaikovsky, A., Ossipenko, F., Slesar, A., Nicolae, D., Belegante, L., Talianu, C.,
854 Serikov, I., Linné, H., Jansen, F., Apituley, A., Wilson, K., de Graaf, M., Trickl, T., Giehl, H., Adam, M.,
855 Comeron, A., Muñoz-Porcar, C., Rocadenbosch, F., Sicard, M., Tomás, S., Lange, D., Kumar, D., Pujadas, M.,
856 Molero, F., Fernandez, A. J., Alados Arboledas, L., Bravo-Aranda, J. A., Navas-Guzmán, F., Guerrero-Rascado,
857 J. L., Granados-Munoz, M. J., Preißler, J., Wagner, F., Gausa, M., Grigorov, I., Stoyanov, D., Iarlori, M., Rizi,
858 V., Spinelli, N., Boselli, A., Wang, X., Lo Feudo, T., Perrone, M. R., De Tomasi, F., and Burlizzi, P.:



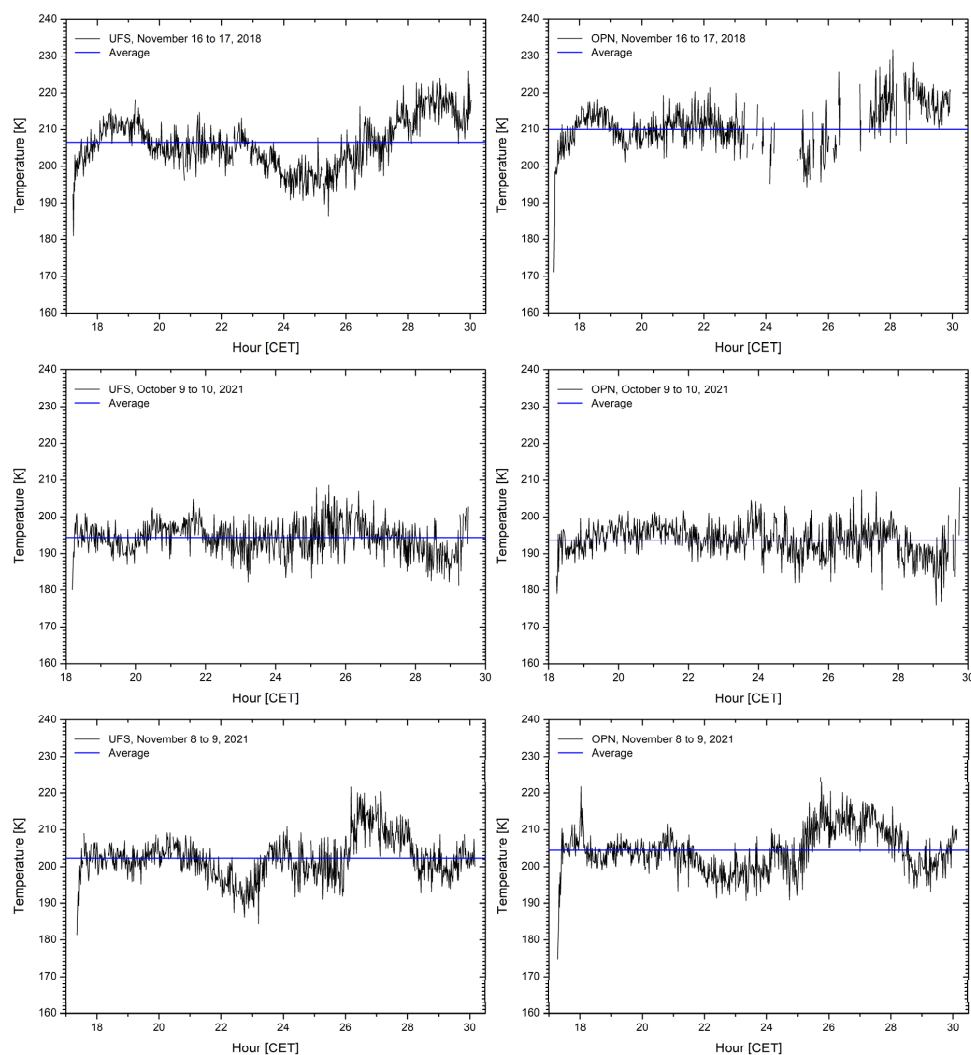
- 859 EARLINET instrument intercomparison campaigns: Overview on strategy and results, *Atmos. Meas. Tech.*, 9,
860 1001–1023, 2016.
- 861 Wing, R., Hauchecorne, A., Keckhut, P., Godin-Beekmann, S., Khaykin, S., McCullough, E. M., Mariscal, J.-F.
862 and d’Almeida, E.: Lidar temperature series in the middle atmosphere as a reference data set – Part 1: Improved
863 retrievals and a 20-year cross-validation of two co-located French lidars, *Atmos. Meas. Tech.*, 11, 5531–5547,
864 2018a.
- 865 Wing, R., Hauchecorne, A., Keckhut, P., Godin-Beekmann, S., Khaykin, S., and McCullough, E. M.: Lidar
866 temperature series in the middle atmosphere as a reference data set – Part 2: Assessment of temperature
867 observations from MLS/Aura and SABER/TIMED satellites, *Atmos. Meas. Tech.*, 11, 6703–6717, 2018b.
- 868 Wing, R., Godin-Beekmann, S., Steinbrecht, W., McGee, T. J., Sullivan, J. T., Khaykin, S., Sumnicht, G., and
869 Twigg, L.: Evaluation of the new DWD ozone and temperature lidar during the Hohenpeißenberg Ozone
870 Profiling Study (HOPS) and comparison of results with previous NDACC campaigns, *Atmos. Meas. Tech.*, 14,
871 3773–3794, 2021
- 872 Wüst, S., Bittner, M., Yee, Y.-H., Mlynchak, M. G., and Russell, J. M. III: Variability of the Brunt–Väisälä
873 frequency at the OH* layer height, *Atmos. Meas. Tech.*, 10, 4895–4903, [https://doi.org/10.5194/amt-10-4895-](https://doi.org/10.5194/amt-10-4895-2017)
874 2017, 2017.
- 875 Wüst, S., Bittner, M., Yee, J.-H., Mlynchak, M. G., and Russell III, J. M.: Variability of the Brunt–Väisälä
876 frequency at the OH*-airglow layer height at low and midlatitudes, *Atmos. Meas. Tech.*, 13, 6067–6093,
877 <https://doi.org/10.5194/amt-13-6067-2020>, 2020.
- 878 Wüst, S., Bittner, M., Espy, P. J., French, P. J., and Mulligan, F.- J.: Hydroxyl airglow observations for
879 investigating atmospheric dynamics: results and challenges, *Atmos. Chem. Phys.*, 23, 1599–1618,
880 <https://doi.org/10.5194/acp-23-1599-2023>, 2023.
- 881 Xu, J., She, C. Y., Yuan, W., Mertens, C., Mlynchak, M., and Russell, J.: Comparison between the temperature
882 measurements by TIMED/SABER and lidar in the midlatitude, *J. Geophys. Res.*, 111, A10S09, doi:
883 10.1029/2005JA011439, 11pp., 2006.
- 884



885 **Figures:**

886

887



888 **Fig. 1.** Examples of GRIPS night-time temperature series at UFS (left column) and Oberpfaffenhofen (OPN,
889 right column) in November 2018, October 2021 and November 2021. There is relatively good agreement for the
890 first two measurements, but in the third case some differences are seen between the results of the two stations.
891 Gaps are due to cloud coverage. The uncertainties at the beginning and the end of a given night is high due to
892 additional daylight.

893

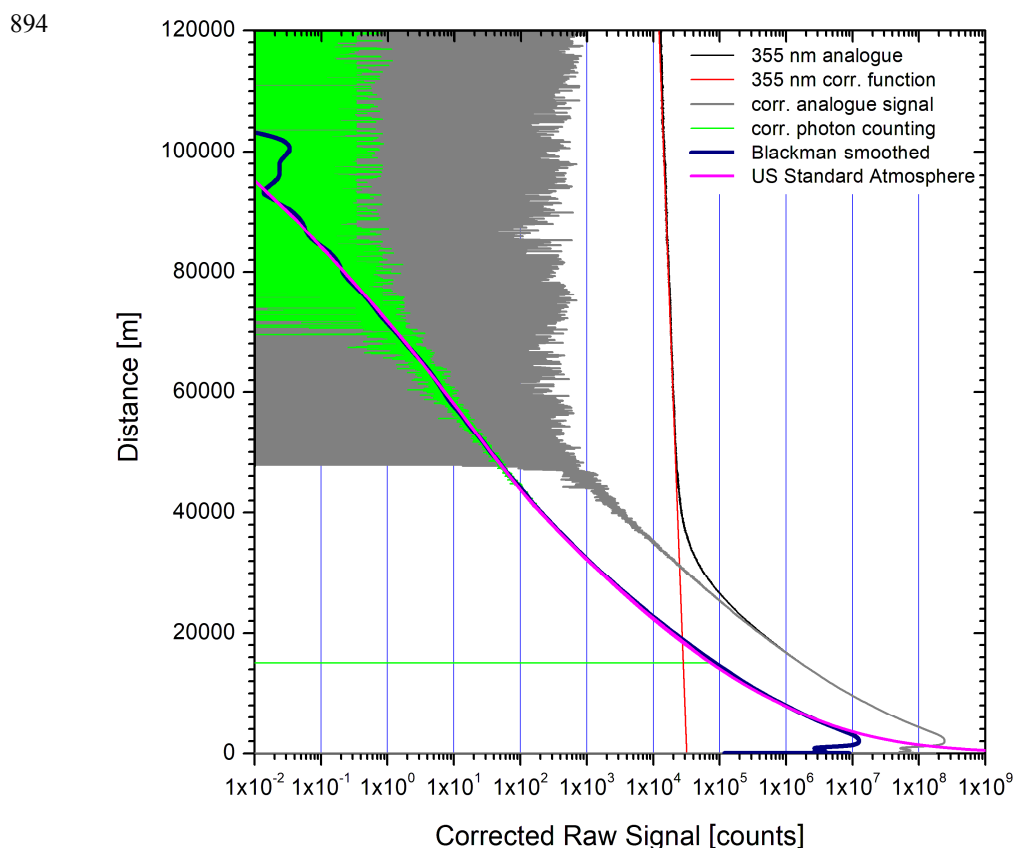


Fig. 2. 355-nm backscatter signals accumulated on 9 October 2021 between 23:05 and 24:01 CET (67171 laser shots) with the transient digitizer and the photon-counting system; the photon-counting signal starts at 15 km due to a data-acquisition delay (see horizontal green line). Above 100 km just occasionally a single photon was detected (see scale). The combined signal (after calibrating the analogue signal to counts) from both recorders is smoothed with a Blackman-type numerical filter with a range quadratically growing with altitude (blue; see text). For comparison also a synthetic lidar signal simulated with data from the U.S. Standard Atmosphere is shown.

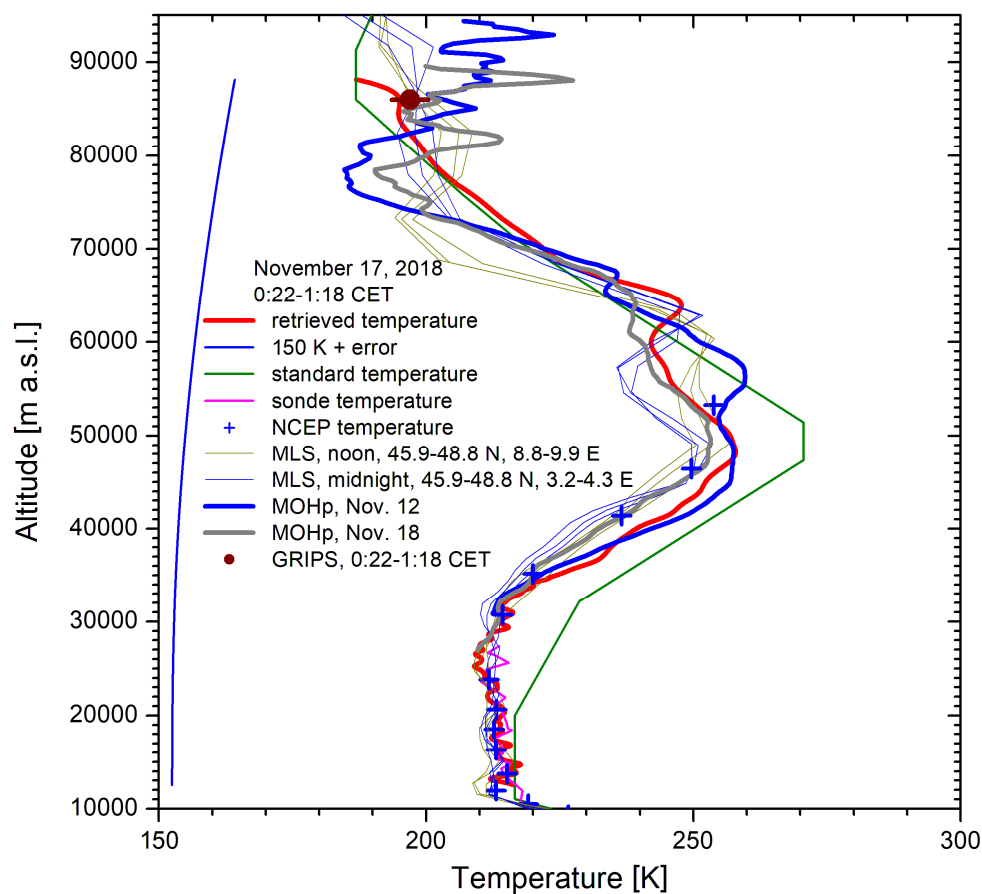
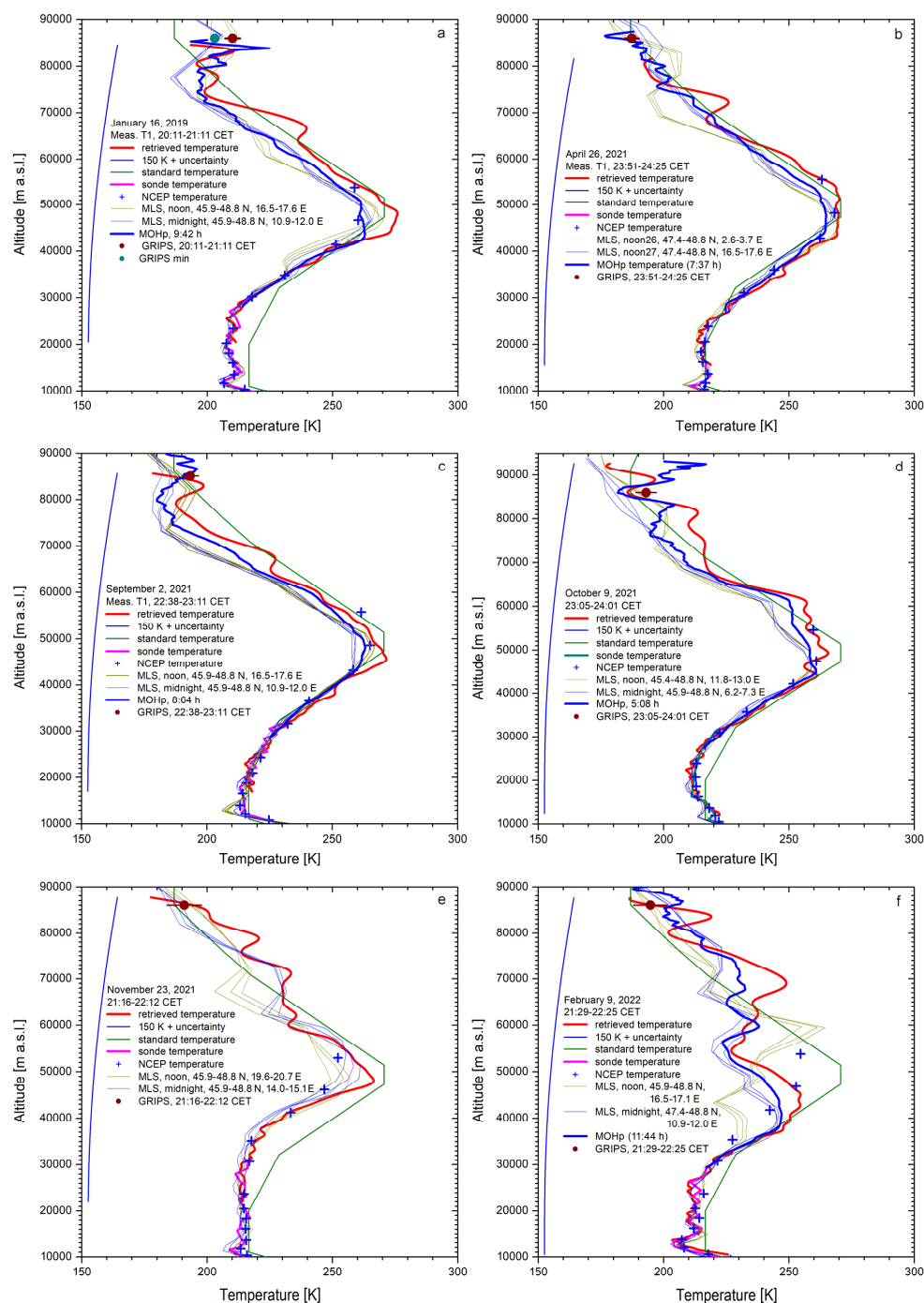


Fig. 3. Temperature measurements on 17 November 2018, compared with data and profiles from other sources (see text).

Please, print this figure larger than in single-column format to allow visualizing the details.



909



910

Fig. 4. Six examples of comparisons of temperature profiles from the UFS lidar with the results of other instruments (for details see legends and text). For a given day, we show both the “midnight” and the “noon” MLS profiles. In the case of Panel (b) the “midnight” MLS profiles are missing and those of the neighbouring two “noon” overpasses are displayed.

914

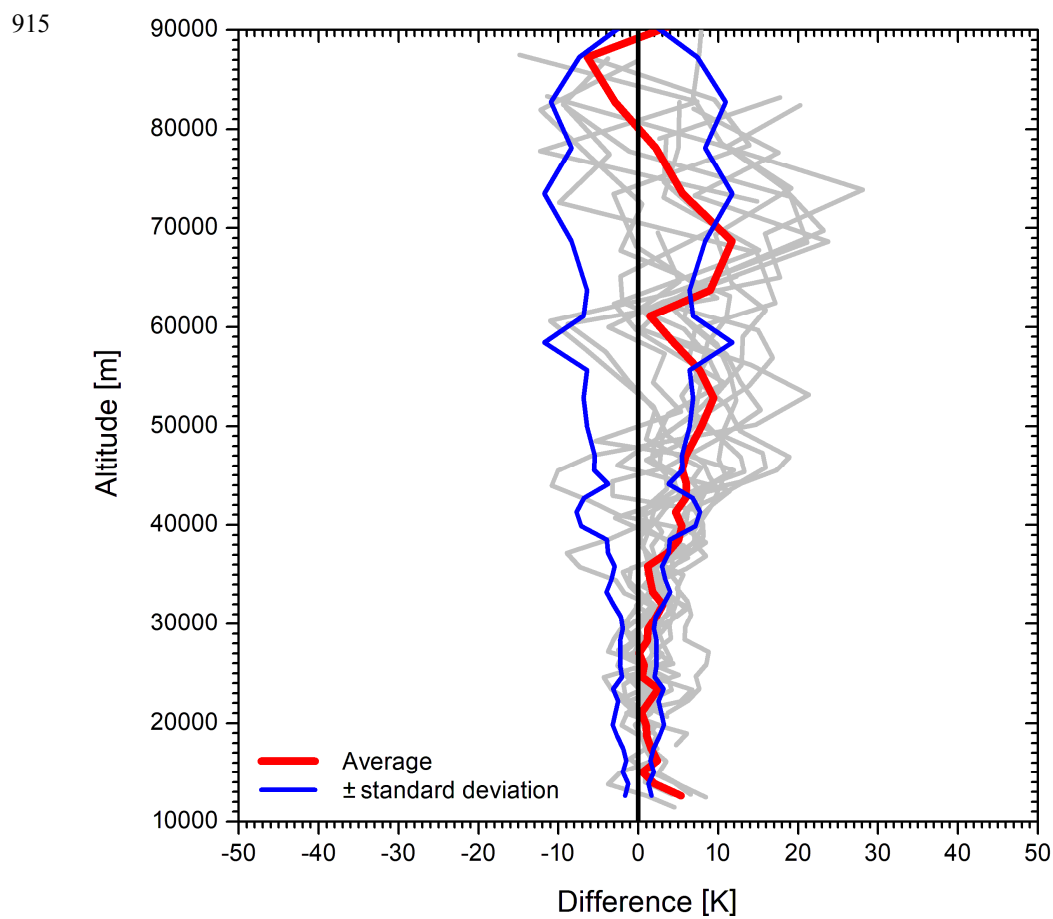
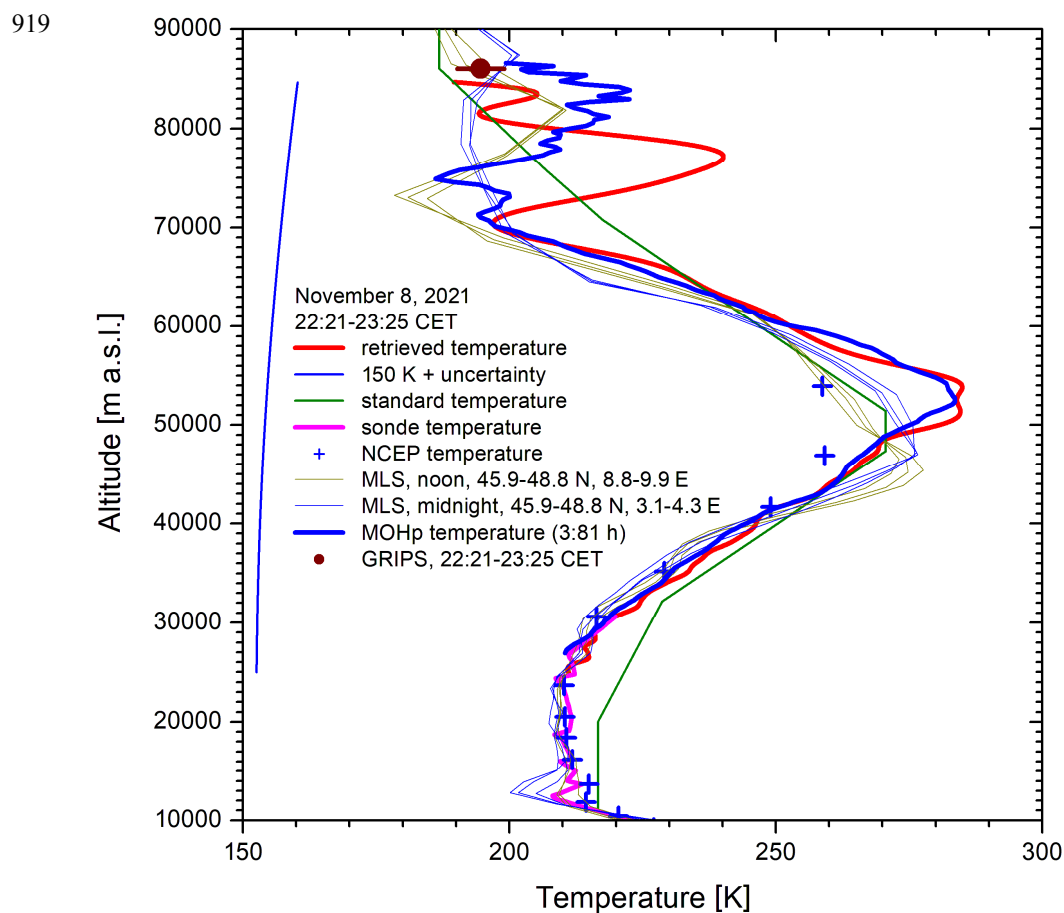


Fig. 5. Differences of the 14 temperature profiles of the UFS lidar and the corresponding measurements of MLS for 47.35° N (grey lines) together with their averages (red line) and standard deviations (blue lines).



920 **Fig. 6.** Comparison of the temperature profile from the UFS lidar on 8 November 2021 with the results of other
 921 instruments; here, we observe an almost perfect agreement with the T profile from MOHp up to 70 km, that was
 922 taken during a rather short period between 22:30 CET and 1:49 CET, i.e., almost synchronously to the
 923 measurement at UFS.

924

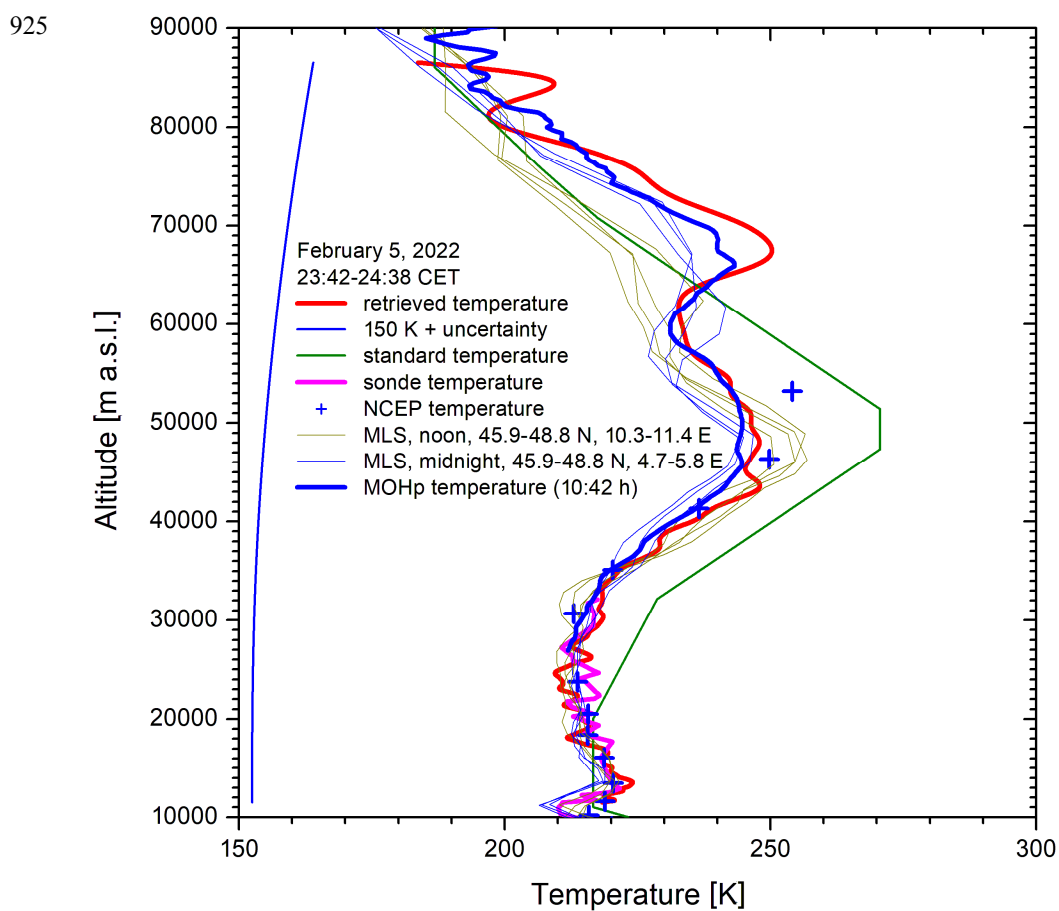
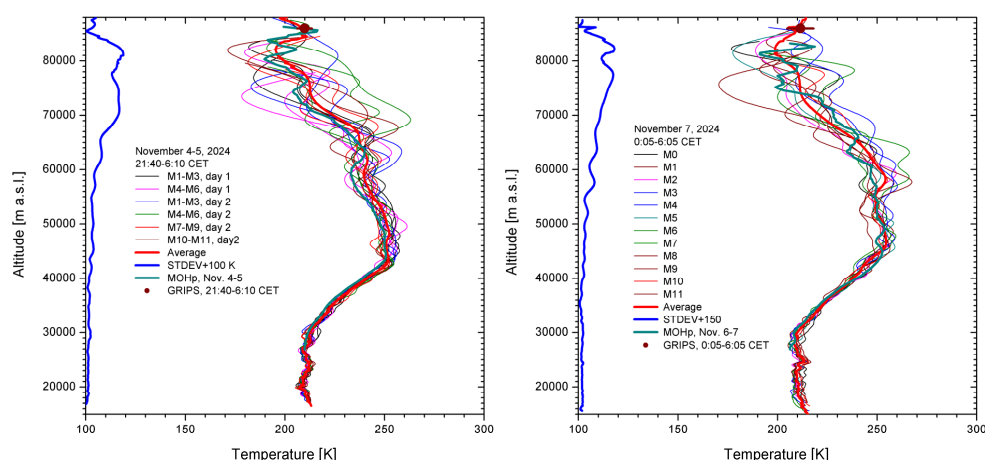


Fig. 7. Comparison of the temperature profile from the UFS lidar on 5 February 2022 with the results of other instruments; here, we observe an almost perfect agreement with the T profile from MOHp, showing rather good agreement up to 65 km. No OH* measurements are available for that night. The reference temperature was chosen to match the MOHp temperatures above 77 km (disregarding the ringing).



931



932

Fig. 8. Two of the four night-time series of the UFS 0.5-h temperature profiles in November 2024, compared with the all-night T profiles obtained at MOHp and the GRIPS average during the lidar measurement periods:

933

Left panel: 4 November 2024 (start at 21:40 CET) to 5 November 2024 (end at 6:10 CET, beginning of the dawn); groups of three subsequent profiles (M means measurement) are presented share the same colour in order to reduce confusion.

936

Right panel: 7 November 2024 (0:05 to 6:05 CET); all profiles for measurements 0 to 11 are coloured differently, from black and violet to red.

937

The standard deviations (STDEV) are shown in blue after adding 100 K.

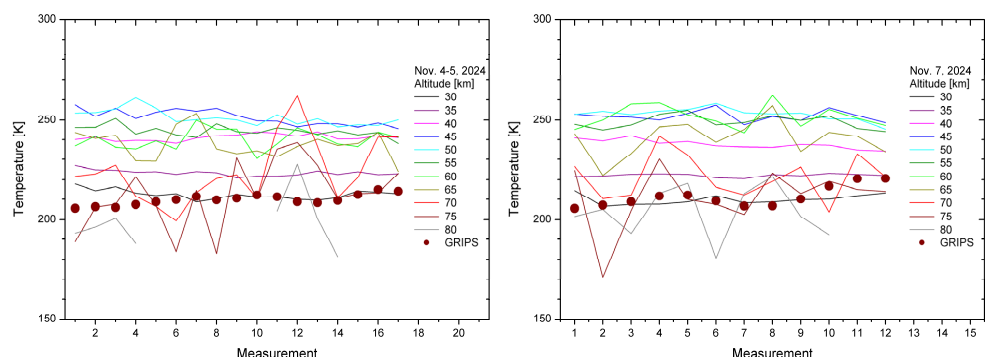
938

939

940

941

942



943

Fig. 9. Time series for the two examples shown in Fig. 8 for selected altitudes listed in the legend, together with half-hour averages of the GRIPS temperatures; here, the measurements are labelled from the beginning to the end of the night-time series.

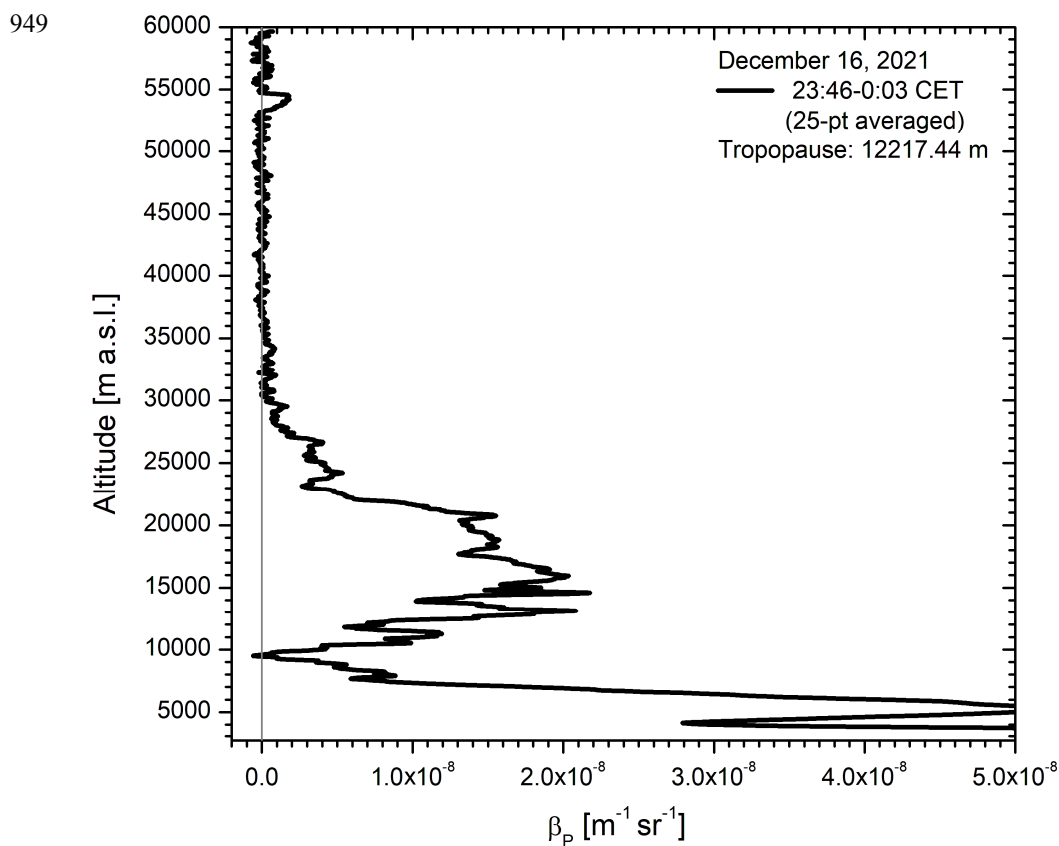
944

945

946

947

948



950 **Fig. 10.** 532.2-nm aerosol backscatter coefficients β_p from a night-time measurement with the UFS stratospheric

951 aerosol lidar showing a strange peak at 54 km.

952

953